https://doi.org/10.5194/gchron-2020-33
Preprint. Discussion started: 24 November 2020

Uranium incorporation in fluorite and exploration of U-Pb dating

Louise Lenoir[1], Thomas Blaise[1], Andréa Somogyi[2], Benjamin Brigaud[1], Jocelyn Barbarand[1], Claire Boukari[1], Julius Nouet[1], Maurice Pagel[1]

[1]Université Paris-Saclay, CNRS, GEOPS, Orsay, 91405, France
[2]Université Paris-Saclay, Synchrotron SOLEIL, Saint-Aubin, 91190, France

Correspondence to: Louise Lenoir (louise.lenoir@universite-paris-saclay.fr)

Abstract. The age of ore deposits constitutes a decisive element in understanding their formation. Deciphering their precise chronology may be a challenge in the absence of mineral phases that can be dated by conventional geochronometers. Fluorite is very common either as the major or accessory mineral in a wide variety of ores and may provide information regarding the origin and timing of mineralizing fluid flows. In this contribution, we explore U-Pb dating on fluorite crystals from the world-class carbonate strata-bound fluorite ore of Pierre-Perthuis in Burgundy (Morvan massif, France). Uranium distribution within fluorite is mapped using induced fission-track and Synchrotron radiation X-Ray Fluorescence nano-imaging, showing that higher uranium content is measured in an overgrowth of fluorite (Fl$_{og}$) as a discrete band. Preservation of a micrometer-thick zonation in U, associated with other substituted elements such as Sr, Y, Fe and Zr implies that neither solid-state diffusion nor dissolution-recrystallization did occur. These U-bearing external fluorite overgrowths contain solid inclusions of about 30 µm globular pyrite crystals with a mean δ^{34}S of –23.6 ± 0.4‰ $_{\text{V-CDT}}$. We propose that the U incorporation in the fluorite lattice results from its reduction mediated by H_2S release during bacterial sulphate reduction. Fl$_{og}$ generation sampled and analyzed by LA-ICP-MS on four different crystals provides identical U-Pb ages within the limits of analytical uncertainty. Considered altogether, these four crystals yield an age estimate of 40.0 ±1.7 Ma, not corrected for matrix-related elemental fractionation. Our results show that fluorite LA-ICP-MS U-Pb geochronology has potential for dating distinct crystal growth stages, although further research should be conducted to evaluate its accuracy.

1 Introduction

Sedimentary rocks lying unconformably upon a crystalline basement may host large concentrations of authigenic F, Ba, Pb, Zn and U minerals that are of economic interest (Boiron et al., 2002; Gigon et al., 2020; Gigoux et al., 2015; Leach et al., 2005; Sizaret, 2006). These unconformity-related deposits are usually the result of multiple fluid flows inducing mineral dissolution-recrystallization, remobilization and precipitation (Chi et al., 2018; Walter et al., 2018). Knowing the timing of these successive fluid flows is essential for building robust genetic models for mineral deposition. Fluorite, one of the 27 critical raw materials defined as crucial for the economy of the European Union (European Commission, 2017), is commonly associated in mineral assemblages in veins or strata-bound deposits. Fluorite Sm-Nd geochronology (Galindo et al., 1994; Dill et al., 2011) might help to reconstitute the geological scenario which led to the mineral deposition, together with other direct radiometric dating of authigenic phases, either by bulk dissolution (e.g., Rb-Sr on sphalerite (Nakai et al., 1993), Re-Os on molybdenite (Markey et al., 1998; Stein et al., 2001) and Re-Os on pyrite (Cardon, 2007; Mathur et al., 2000)) or by in situ sampling and analysis (e.g., Ar-Ar on adularia (Cathelineau et al., 2012; Mark et al., 2005) Ar-Ar on Mn oxides (Deng and Li, 2017) or U-Pb on uraninite (Alexandre et al., 2009; Martz et al., 2019)).

However, it is frequent that fluorite Sm-Nd geochronology produces errorchrons, and additionally, when the age estimation is considered as geologically consistent, results may be unreliable due to poor analytical precision. Moreover, it is sometimes difficult to interpret Sm-Nd ages when they are obtained from the bulk dissolution of a crystal fragment that may be composed of several growth stages. To overcome these issues, a non-radiometric method based on the acquisition of chemical remnant magnetization in fluorite has been developed and employed to date fluorite deposits in areas where the geodynamic evolution and the apparent polar wander path are well documented (Kawasaki and Symons, 2008; Symons, 1994; Symons et al., 2017). Along with other elements, fluorite accepts the incorporation of uranium and lead in its crystal lattice in substitution for Ca^{2+} (typically at low concentrations, from a few ppm to a few ‰, (Piccione et al., 2019)). As a result, fission-track (Grønlie et al., 1990) and (U-Th)/He (Evans et al., 2005; Wolff et al., 2015) thermochronology have been tested in fluorite. Wolff et al., (2016) show that He diffusion in fluorite varies depending on metal substitution in the crystal lattice.

In recent years, in situ U-Pb geochronology has been successfully applied to a growing number of mineral matrices, including calcite and dolomite (Burisch et al., 2017), hematite (Walter et al., 2018), opal (Nuriel et al., 2019), cassiterite (Moscati and Neymark, 2020), Mn-rich chrysocolla and pseudomalachite (Kahou et al., 2020), epidote (Peverelli et al., 2020), nacrite and fluorite (Piccione et al., 2019). Piccione et al., (2019) reported for the first time LA-ICP-MS U-Pb ages acquired on fluorite that are consistent with those of adjacent nacrite crystals, showing that fluorite U-Pb geochronology can constrain the timing of fluid flows, providing favorable U/Pb. However, the incorporation and retention of U and Pb in the crystal structure of CaF_2 are very poorly documented, hence currently limiting the reliability of fluorite U-Pb dating. Moreover, compared to other common lead-bearing minerals, fluorite sampling by laser ablation presents some additional analytical challenges, such as laser-induced damage (De Bonis et al., 2014; Jia et al., 2005; Rafique et al., 2012) and ejection of solid fragments causing variable ablation rates (Gogoll et al., 1996).

The aim of this study is to examine the spatial distribution of uranium and lead and to further explore small-scale LA-ICP-MS U-Pb geochronology in fluorite crystals. The unconformity-related F-Ba ore in Pierre-Perthuis (Morvan massif, France) was chosen as a case study. This ore has been investigated in previous studies (Gigoux et al., 2015, 2016) and a generation of macroscopic geodic fluorite has been dated at 130 ± 15 Ma by Sm-Nd (Gigoux et al., 2015). As in many other F-Ba deposits, the most commonly used geochronometers are lacking in Pierre-Perthuis, making it an ideal target for testing fluorite U-Pb dating. Through the use of various petro-geochemical investigations involving multiple analytical methods, including induced fission-track mapping, Synchrotron radiation X-Ray Fluorescence nano-imaging, secondary ion mass spectrometry and LA-ICP-MS, this paper will address the following questions:

- How are U and Pb spatially distributed within micrometer-thick fluorite growth bands?
- How is uranium incorporated in fluorite?
- Are U and Pb effectively retained in fluorite?
- Can we use fluorite U-Pb geochronology to gain knowledge of the chronology of fluid flows?

2 Geological settings

The studied area is located at the interface between the Paris Basin and the French Massif Central (FMC), about 200 km south east of Paris. The Paris Basin is an intracratonic sedimentary basin that formed above Cadomian and Variscan basement rocks (Guillocheau, 2000). The FMC was structured during the Variscan orogeny (Lardeaux et al., 2014; Vialette, 1973). The northern edge of the FMC corresponds to the Morvan Massif, made up mostly of granitic rocks emplaced during the Early and Late Carboniferous (Lardeaux et al., 2014; Vialette, 1973). The northern Morvan basement is composed of three granitic units namely the *Avallon, Lormes* and *Les Settons* and a metamorphic unit (Lower Gneiss Unit). The Pierre-Perthuis ore is spatially related to an unconformity between the *Avallon* granite basement and the Late Triassic sediments on the northwestern part of the Morvan Massif (Figure 1a). Two main geological units compose the Pierre-Perthuis outcrop: (1) the *Avallon* two-mica granite which shows a weathered zone of about 0.5 to 3 m thickness at its top, and (2) 4 to 8 m of silicified dolostone that corresponds to the *Assise de Chitry* Formation (Fm), a Carnian/Norian dolomite formation (235–208 Ma), silicified after the deposition (Figure 1b). The main fluorite mineralization form euhedral (cubic habits) fluorite crystals dispersed within the silicified dolomite rock. A second occurrence forms centimeter cubic fluorite in geodic cavities that crystallized under relatively stable temperatures of 80-100°C (Gigoux et al., 2016). These fluorite mineralizations are complemented by two barite stages (an early small blade-shaped barite stage and a late fan-shaped pink barite stage), three quartz stages (a microcrystalline stage responsible for the silicification of the *Assise de Chitry* Fm co-precipitated with chalcopyrite followed by a quartz fringe stage, and a late granular stage) and at least four sulphide stages.

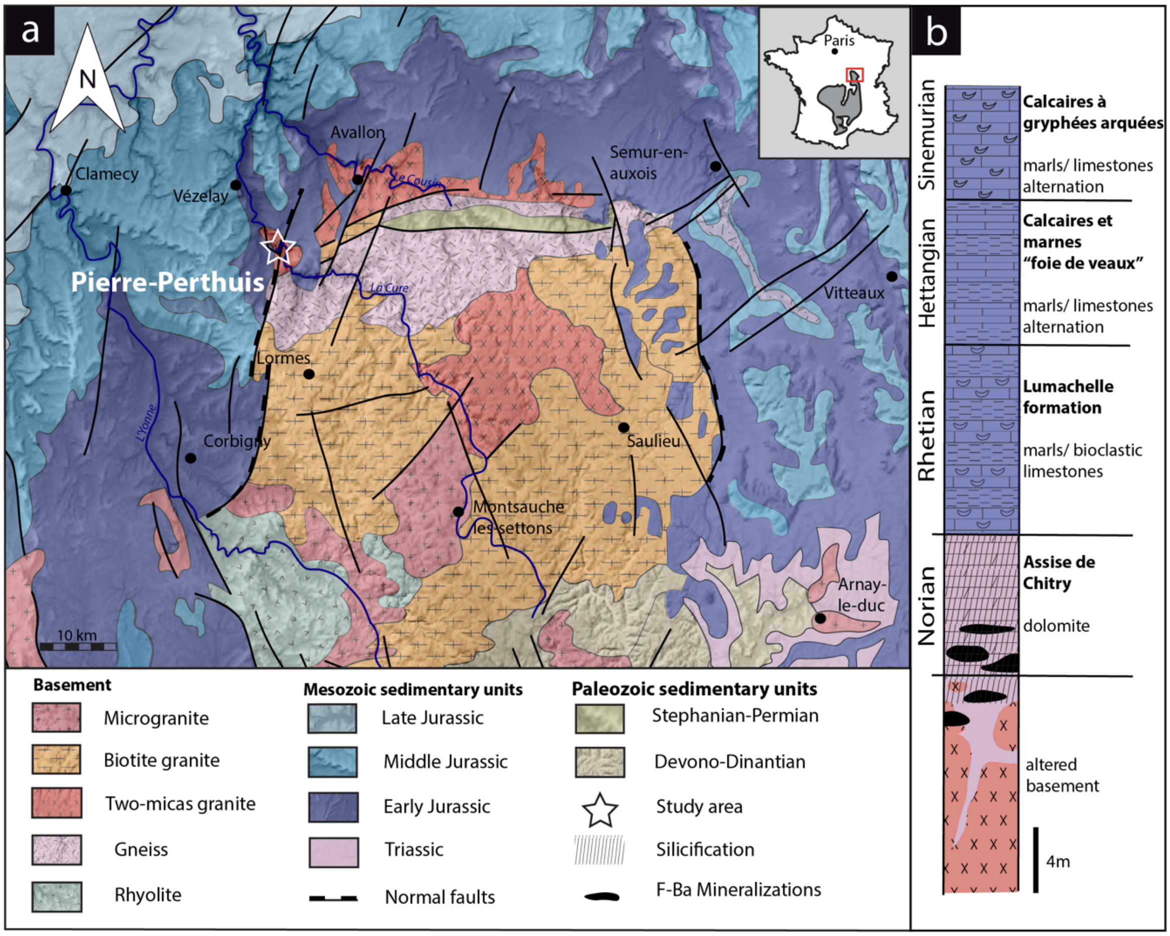

Figure 1: (a) Geological map of the Morvan Massif with the location of the strata-bound fluorite ore of Pierre-Perthuis (modified according to the 1/1.000.000 geological map, BRGM) and its (b) stratigraphic log modified according to Soulé de Lafont and Lhégu (1980).

3 Materials and methods

3.1 Sampling strategy

The Pierre-Perthuis district is composed of three areas: (1) *Bois Dampierre*, (2) *Bois de l'Epenay* and (3) *La roche percée* (Figure 2). All samples were collected at the Pierre-Perthuis ore from outcropping rocks in the weathered granite (Figure 1c) close to the sedimentary cover and are summarized in Table 1.

https://doi.org/10.5194/gchron-2020-33
Preprint. Discussion started: 24 November 2020

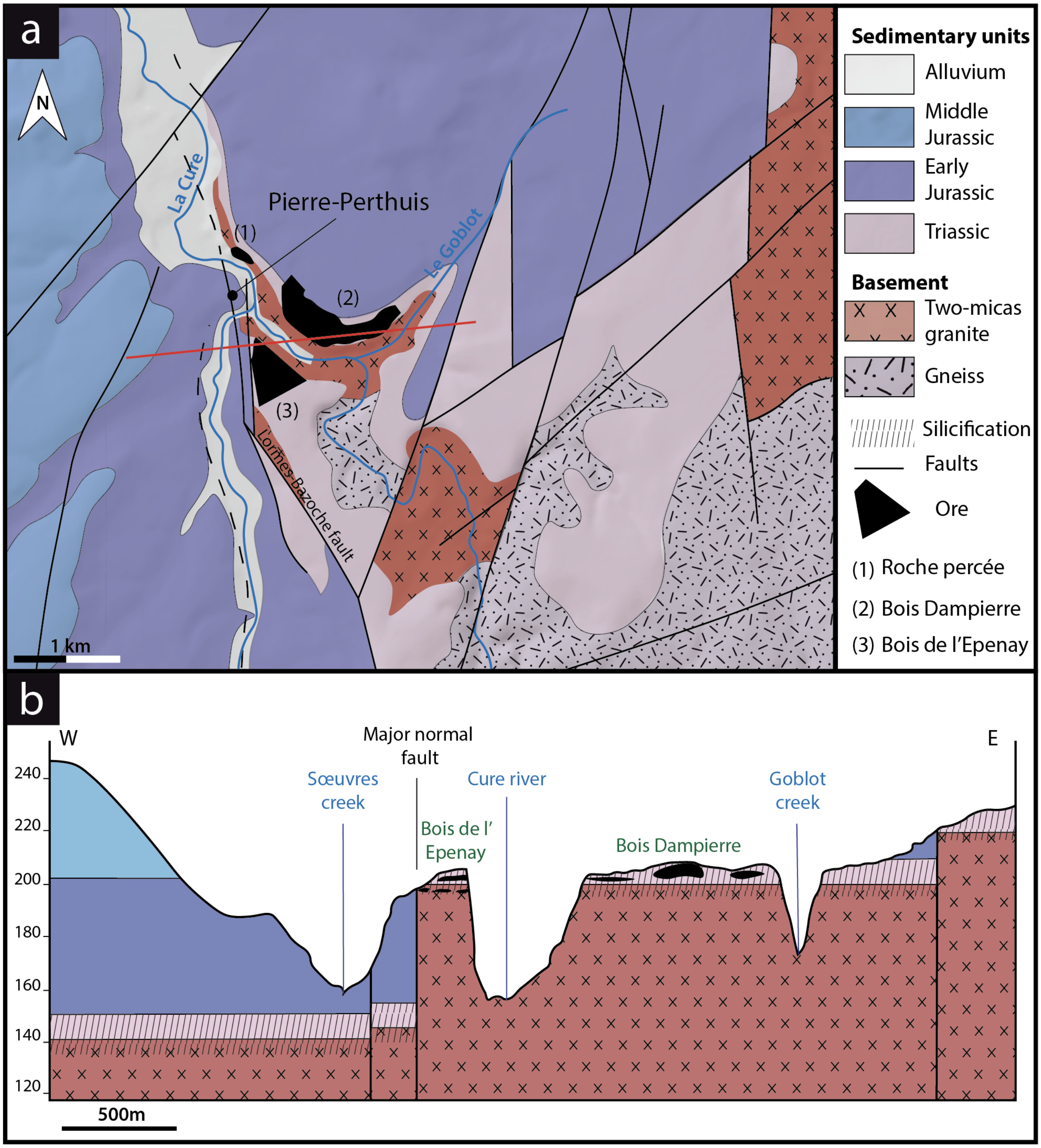

Figure 2: a) Location of the mineralized outcrops at Pierre-Perthuis and b) a W-E geological profile localized on the geological map by the red line, modified according to the 1/50.000 geological map of *Avallon* (Horon et al., 1966), (Gigoux et al., 2016; Soulé de Lafont and Lhégu, 1980b). 100

Sample Name	Location			Applied Method						
	Geographic sector	Lat. X	Long. Y	δ^{34}S by SIMS (‰$_{\text{V-CDT}}$)		U-Pb dating by LA-ICP-MS (Ma)		Fission track mapping		Scanning SR-XRF
				δ^{34}S	2σ	Age	2σ	Tracks nb	Area(µm^2)	
PP18S3	Bois Dampierre	47.43	3.792	–24.2	0.3	N.D.	N.D.	N.D.	N.D.	N.D.
PP18S7	Bois Dampierre	47.43	3.792	–23.6	0.3	N.D.	N.D.	N.D.	N.D.	Zr, Fe, Th, Sr, Pb, Y, U
PP18S15	Bois Dampierre	47.43	3.792	N.D.	N.D.	N.D.	N.D.	N.D.	N.D.	Ca, Fe, Th, Sr, Pb, Y, U
PP1802	Bois Dampierre	47.43	3.792	N.D.	N.D.	40.8	3.4	1276	$51.5.10^3$	N.D.
PP1801	Roche percée	47.436	3.784	N.D.	N.D.	N.D.	N.D.	196	24.10^3	N.D.
PPVi2	Roche percée	47.435	3.786	N.D.	N.D.	38.7	1.8	N.D.	N.D.	N.D.
PPVi5	Roche percée	47.435	3.786	N.D.	N.D.	41.1	2.2	N.D.	N.D.	N.D.
PP15	Bois de l'Epenay	47.431	3.786	N.D.	N.D.	41.8	2.8	N.D.	N.D.	N.D.

Table 1: Sample location, sulfur stable isotopic composition of pyrite, fluorite U-Pb age, fission track and Scanning SR-XRF of fluorite. (N.D. = not determined)

3.2 Petrographic observations

Polished thin sections were observed with optical microscopy in transmitted and reflected light, and under cathodoluminescence (CL) equipment composed of a BX41 microscope coupled to a cold cathode from NewTec operating at 12 kV and 200-300 µA and a Qicam Fast 1394 digital camera. More details about the cathodoluminescence activators and inhibitors in fluorite can be found in Baele et al., (2012) and Kempe et al., (2002). Uncoated polished thin sections were also observed and analyzed by scanning electron microscopy (SEM, Phenom X Pro) using a charge compensation sample holder in backscattered electron mode (BSE). Images were produced at an acceleration voltage of 15 keV. Semi-quantitative elemental compositions were measured through energy dispersive X-ray spectrometry (EDS) at an acceleration voltage of 15 keV and an accumulation time of 30 s.

3.3 Uranium distribution mapping

To map the uranium distribution in fluorite crystals of the Pierre-Perthuis ore, the fission track cartography based on the induced fission of ^{235}U was carried out using the external detector method (Gleadow, 1981). Fluorite crystals were mounted in an epoxy resin and polished. Polished sections were covered by muscovite detectors in close contact and irradiated in the Research Neutron Source Heinz Maier-Leibnitz (FRM II) of the Technical University of Munich (Garching, Germany). Thermal neutron fluence was 1 x 10^{16} n/cm^2. Track densities are calibrated using the standard reference glass CN5 with a total U concentration of 12.17 ppm. After irradiation, the external detectors were detached and etched in 48% HF at 20 ± 1°C for 20 minutes. Induced fission tracks revealed on detectors were observed and counted using a LEICA DMLM optical microscope in transmitted light with a x1000 magnification.

3.4 Scanning Synchrotron radiation X-Ray Fluorescence nano-imaging

Fluorite crystals were mounted in an epoxy resin, polished on both sides to a thickness of a hundred microns and cut into 5mm-edge squares. These preparations were fixed on Teflon rings and positioned perpendicularly to the incoming X-ray beam.

Seven fluorite samples were scanned by Synchrotron radiation X-ray fluorescence (SR-XRF) using the Nanoscopium hard X-ray nanoprobe beamline (Bergamaschi et al., 2017; Somogyi et al., 2015) of Synchrotron SOLEIL (Université Paris-Saclay, Saint Aubin, France). Elemental distribution mapping was acquired from these polished sections in different areas at a spatial resolution varying from 50 nm to 1 µm and with an integration time per pixel varying from 150 ms to 20 ms. The 18 keV monochromatic X-ray beam was focused on the crystal samples by a Kirckpatrick-Baez nano-focusing mirror. This excitation energy of 18 KeV was chosen farther away from the U-L$_3$ absorption edge (17.168 keV) in order to avoid the overlapping of the U-L3 X-ray lines and the Compton scattering peak of the incident X-ray beam from the sample. This allows the optimization of the analytical sensitivity of U due to the reduced spectral background below the U-L$_3$ lines. To obtain nanometer-scale resolution elemental maps on mm^2 sized samples, a fast-continuous scanning technique (FLYSCAN) has been employed (Lanzirotti et al., 2010; Medjoubi et al., 2013). Full XRF spectra were collected at each pixel of the scans by two silicon drift detectors of 50 mm^2 useful area (KETEK H50, KETEK GmbH) used with XMAP (XIA LLC) fast digital multichannel analyzer cards. The XRF detectors were placed at 20° relative to the sample surface (Somogyi et al., 2015).

The high-resolution scans consisted of 100 000 - 300 000 individual XRF spectra corresponding to an XRF spectrum at each image pixel. In order to treat this data-set, as a first step we used the XRF sum-spectrum of the entire scanned area to identify the main elements present. The distribution maps of these elements were reconstructed by an in-house Matlab® code. Because the scanned areas sometimes included different mineral matrices (fluorite and pyrite), or successive growth bands of distinct chemical composition in the same mineral, sub-zones were defined by the Matlab® code from the elemental distribution maps in order to extract the average XRF spectrum corresponding exclusively to the targeted mineral matrix or growth band. These sub-zones, or regions of interest (ROIs), were selected by using ImageJ® software (Schneider et al., 2012). The mean XRF spectra of the ROIs was fitted using PyMCA® software (Solé et al., 2007). This allowed us to identify additional elements, present only in tiny areas or in small quantities (e.g., Th), and as such not detectable in the sum-spectrum of the whole sample area. As a second step, the elemental distribution maps of all the identified elements were reconstructed by correcting for spectral overlaps depending on the intensity ratios of the X-ray lines.

3.5 Sulfur stable isotope composition of pyrite

Sulfur isotopes were measured by Secondary Ion Mass Spectrometry (SIMS) using a multi-collectors CAMECA IMS1270 E7 microprobe at the *Centre de Recherches Pétrographiques et Géochimiques* (CRPG, Université de Lorraine and CNRS) in Nancy (France). Samples that were already prepared for synchrotron XRF-spectromicroscopy were re-used. They were glued on a glass slide, then coated with a layer of 30 nm of Au. To accurately locate the SIMS analysis, petrographic observations using reflected light microscopy were carried out before and after gold plating. Pyrite inclusions in fluorite were sputtered with a 10 kV Cs^+ primary ion beam with a current of 2.7 nA. A normal-incidence electron gun was used for charge compensation. $^{32}S^-$ and $^{34}S^-$ secondary ions were detected in multi-collection mode using two Faraday cups. Samples were pre-sputtered for 120 seconds with a beam raster of 20 x 20 µm prior to signal acquisition to minimize surface contamination. Faraday cup backgrounds were measured during the pre-sputtering before each analysis and then used for correcting the data. Typical count rates of $^{32}S^-$ and $^{34}S^-$ were of 4.8×10^8 counts per second (cps) and 2×10^7 cps respectively, during 30 cycles of 4.96 seconds acquisition time. The spot size was about 15 µm in diameter. A nominal mass resolution (M/ΔM) of 4998 was used to resolve interference with hydrides.

A Sierra Pyrite sample was used as an internal matrix-match standard to correct the sulfur isotopic ratio (Table 2). Data was integrated as a $^{32}S/^{34}S$ ratio ($\delta^{34}S$ in ‰) and referenced to the Vienna-Canyon Diablo Troilite (V-CDT) scale (Ding et al., 2001). Homogeneity of the Sierra Pyrite has been documented by LaFlamme et al., (2016) by three analytical techniques (EPMA: Electron Probe Micro Analyser, Wavelength-Dispersive X-Ray Spectroscopy-maps and SEM-BSE) and its $\delta^{34}S$ measured by SIMS at 2.17 ± 0.08 $‰_{V\text{-}CDT}$. Measurements were carried out through daily sequences consisting of 5 analyses of matrix-match reference material followed by spots on unknown samples. For the first session, Sierra pyrite was measured at 0.94 ± 0.02 $‰_{V\text{-}CDT}$, and at 0.92 ± 0.02 $‰_{V\text{-}CDT}$ for the second analytical session. Instrumental mass fractionation (IMF) for $^{34}S^-/^{32}S^-$ was quantified during each analytical session using all the replicated analyses of the matrix-match standard. During the first session the IMF was –1.23 ± 0.34 $‰_{V\text{-}CDT}$, and –1.25 ± 0.28 $‰_{V\text{-}CDT}$ for the second. Final uncertainties are reported at a 95% confidence level (2σ), propagating the systematic uncertainty of primary reference material Sierra pyrite (3.7 %, LaFlamme et al., 2016), and the propagated correction for instrument mass fractionation through the analytical session by quadratic addition.

Date	Reference material	$\delta^{34}S$ (‰V-CDT) LaFlamme et al., 2016	Sierra Pyrite 2σ error (‰V-CDT)	Standard analyses	$\delta^{34}S$ measured (‰V-CDT)	$\delta^{34}S$ 2σ error (‰V-CDT)	Instrumental mass fractionation	IMF 2σ error (‰V-CDT)
12/11/2019	Sierra Pyrite	2.17	0.08	5	0.94	0.02	–1.227	0.34
12/13/2019				5	0.92	0.02	–1.252	0.28

Table 2: Data for Sierra Pyrite reference material.

3.6 In situ U-Pb geochronology

U and Pb isotopic compositions were measured for 4 fluorite samples showing fluorite overgrowth (Fl_{og}): (1) PPVi2 (n = 16), (2) PPVi5 (n = 20), (3) PP1802 (n = 30) and (4) PP15 (n=26), using a 193 nm excimer laser (Teledyne, Photon Machines) coupled to a Thermo Scientific™ Sector Field Inductively Coupled Plasma Mass Spectrometer (SF-ICP-MS) ELEMENT XR (ThermoFisher Scientific, Waltham, USA) at the Geosciences laboratory (GEOPS) of the University Paris-Saclay.

The overall analytical procedure is derived from LA-ICP-MS U-Pb geochronology of carbonates (Roberts et al., 2020), developed at the University of Paris-Saclay for calcite (Brigaud et al., 2020) - see Table A1 of Appendix A for analytical details. The main difference concerns the laser energy needed to ablate fluorite. Indeed, a fluence of 6 J.cm^{-2} was required to ablate our natural fluorite crystals. To properly correct for downhole fractionation (DF) and other sources of laser-induced elemental fractionation (LIEF) on the measured $^{206}Pb/^{238}U$ ratios, a fluorite primary reference material (RM) should be used. However, such a fluorite RM does not exist yet. Thus, similarly to Piccione et al., (2019), we used a calcite RM, the Permian Reef Complex Walnut Canyon WC-1 (Roberts et al., 2017) as the primary reference material. We highlight that our fluorite U-Pb ages are thus not corrected for matrix-related elemental fractionation. To evaluate the accuracy of our U-Pb ages, we included the analysis of a fluorite sample independently dated by (U–Th–Sm)/He thermochronology (Wolff et al., 2016). It corresponds to a sodium-and Rare Earth Element (REE)-rich green fluorite from the Horni Krupka deposit in Czech Republic (named "HK13") that has been dated by Wolff et al., (2016) at 290 ± 10 Ma.

The laser beam diameter for fluorite unknowns was 85 µm. Fluorite crystals were ablated at a repetition rate of 10 Hz and a fluence of 6.25 J.cm^{-2}. Calcite reference materials, including WC-1 primary standard and two secondary standards that are detailed below, were ablated at a repetition rate of 8 Hz and a fluence of 1 J.cm^{-2}, and a beam diameter of 150 µm. Glass reference materials NIST612 (37.38 ppm U and 38.57 ppm Pb) and NIST614 (0.823 ppm U and 2.32 ppm Pb, Jochum et al., (2011)) were ablated at a repetition rate of 10 Hz, a fluence of 6.25 J.cm^{-2} and a beam size of 40 µm for NIST612 and 110 µm for NIST614.

Each analysis consists of 30 s background acquisition followed by 30 s of sample ablation and 30 s washout. Prior to analysis, each spot was pre-ablated for 7 s at a frequency of 10 Hz and with a fluence of 6.25 J.cm^{-2} for reference material (NIST) and fluorite samples, and at a frequency of 8 Hz and with a fluence of 1 J.cm^{-2} for calcite reference materials. These pre-ablations are over an area larger than the beam diameter to clean the surface (155µm for calcite and NIST612, 110 µm for fluorite and 135 µm for NIST614) and remove potential surficial Pb contamination. The laser-induced aerosol was carried by helium (lage volume at 0. 5 l.min^{-1} and inner cup at 0. 375 l.min^{-1}) from the sample cell to a mixing funnel in which the sample and He are mixed with 0.950 to 1 l.min^{-1} argon to stabilize the aerosol input to the plasma. Signal strength of the ICP-MS was tuned for maximum sensitivity while keeping Th/U at 1.02 and ThO/Th below 0.3% on NIST612. Isotopes ^{206}Pb, ^{207}Pb, ^{208}Pb, ^{232}Th et ^{238}U were acquired with integration times per peak (ms) of 10 ms for ^{208}Pb, ^{232}Th, ^{238}U, of 30 ms for ^{206}Pb and of 40 ms for ^{207}Pb by 70 runs.

We used NIST614 to correct for ^{207}Pb/^{206}Pb fractionation (Jochum et al., 2011). For mass-bias correction of the measured ^{238}U/^{206}Pb ratios, we used the WC-1 calcite reference material (Roberts et al., 2017). Two secondary calcite reference materials were analyzed during the analytical sessions: Duff Brown Tank (DBT), dated at 64.0±0.7 Ma by U-Pb isotope dilution – ICP-MS (Hill et al., 2016), and AUG-B6, a calcite breccia dated by LA-ICP-MS U-Pb at 42.99±1 Ma (Pagel et al., 2018). Internal secondary reference calcite AUG-B6 comes from the Gondrecourt graben (Eastern Paris Basin), part of the European Cenozoic Rift System and has been routinely analyzed for two years at GEOPS (University Paris-Saclay). Measurements have been made by sequences starting with 6 reference material analyses (2 NIST612, 2 NIST614 and 2 WC-1), then a repetition of 10 spots on unknown fluorite followed by 8 reference material analyses (2 NIST614, 2 WC-1, 2 DBT and 2 AUG-B6), 10 spots on unknown fluorite, etc., and ending with 6 reference material analyses (2 NIST612, 2 NIST614 and 2 WC-1). Data was acquired in fully automated mode overnight in two sequences of 336 analyses during about 12 hours of analysis the 19 and 20 December 2019.

Data was reduced in Iolite© using the NIST614 glass as the primary reference material to correct for baseline, for Pb isotope mass bias and for ^{206}Pb/^{238}U instrumental drift over the sequence time (Lawson et al., 2018; Paton et al., 2011). No down-hole fractionation correction is applied in Iolite© (Nuriel et al., 2017). The two-sigma errors in ^{207}Pb/^{206}Pb and ^{206}Pb/^{238}U ratios measured on NIST614 during the analytical session were propagated to the final age uncertainty of fluorite samples by quadratic addition. During the first session, NIST 614 two sigma error on ^{207}Pb/^{206}Pb was 0.31 % and 1.10 % for ^{206}Pb/^{238}U and for the second session the two-sigma errors on ^{207}Pb/^{206}Pb and ^{238}U/^{206}Pb were 2.20% and 0.69% respectively. A signal peak of ^{206}Pb, ^{207}Pb or ^{238}U can occur due to unstable ablation conditions, causing an unusually high ^{206}Pb/^{238}U or ^{207}Pb/^{206}Pb standard error (2 σ), typically greater than 20 %. Thirty-five spots, having 2 σ errors greater than 20 %, were excluded (5 on PPVi5, 7 on PPVi2, 15 on PP1802 and 8 on PP15). Each reduced piece of data is plotted in a ^{238}U/^{206}Pb *versus* ^{207}Pb/^{206}Pb Tera-Wasserburg graph using IsoplotR (Vermeesch, 2018). An isochron is drawn and the isochron age is deduced by the intersection on the concordia. For each sequence, the age and uncertainty of WC-1 reference calcite, following normalization using NIST614 glass, was calculated without further normalization using a Tera-Wasserburg intercept age. Following the

https://doi.org/10.5194/gchron-2020-33
Preprint. Discussion started: 24 November 2020

analytic run, we applied a linear correction factor to correct the $^{206}Pb/^{238}U$ so that the primary WC-1 yields the correct intercept age (*i.e.,* 254.4±6.4 Ma, Roberts et al., 2017). For the first session, we obtained 167.0 ±3.7 Ma for WC-1 with 23 analyses, hence we applied a linear correction factor of 0.656 to correct all $^{206}Pb/^{238}U$ ratios of secondary calcite reference materials and fluorite unknowns. For the second analytical session, WC-1 was dated at 148.0 ±2.3 Ma with 39 analyses. Then, the linear correction factor on the $^{206}Pb/^{238}U$ ratio was 0.582. We fixed the $^{207}Pb/^{206}Pb$ ratio at 0.85 for the common Pb based on Stacey and Kramers, (1975) when we calculated the Tera-Wasserburg intercept age on WC-1 (see (Roberts et al., 2017)). Regarding unknown fluorite samples, Tera-Wasserburg intercept ages are calculated by plotting each spot from a single sample and by applying the linear correction factor found on WC-1 for the corresponding session to correct the $^{206}Pb/^{238}U$ ratios. An age is then calculated without fixing the initial $^{207}Pb/^{206}Pb$ value. Error ellipses of each spots and the error on the Tera-Wasserburg intercept age are 2σ. In each Tera-Wasserburg graph, a first age uncertainty is given that does not include uncertainty propagations (except uncertainties related to the decay constants of ^{235}U and ^{238}U). A second age uncertainty in square brackets is given, by propagating the systematic uncertainty of primary reference material WC-1 age (2.6 %, Roberts et al., 2017) and the two-sigma error of the $^{207}Pb/^{206}Pb$ and $^{206}Pb/^{238}U$ of the analytical session by quadratic addition. Calculated ages for calcite secondary reference materials analyzed during the two sequences were 40.7±1.6 Ma and 44.4±2.0 Ma for AUG-B6 and 63.7±2.2 Ma and 64.6±2.9 Ma for DBT, without fixing the initial $^{207}Pb/^{206}Pb$ ratio. These ages are identical within analytical uncertainty to the ages published for these two calcites (Pagel et al., 2018; Hill et al., 2016, respectively). "HK13" fluorite was dated at 285.9 ± 29.3 [30.9] Ma (Fig. A1 in Appendix A. Even though the isochron is less well defined, this U-Pb age matches the (U-Th-Sm)/He age obtained by Wolff et al., (2016) at 290 ± 10 Ma.

Tera-Wasserburg diagrams of primary and secondary calcite reference materials and metadata for LA-ICP-MS U-Pb ages of fluorite can be found in Fig. A1 and Table A1 of Appendix A and in supplementary material.

4 Results

4.1 Petrographic observations

Three fluorite generations are described below and illustrated in Figure 3a.

The first fluorite stage is composed of 50 µm up to a millimeter-large white cubes disseminated in the altered granite and mainly in the *Assise de Chitry* Fm, named euhedral fluorite Fl_{euh} (Gigoux et al., 2016). These crystals may sometimes form centimeter-sized patches (Figure 3a).

The second stage fills pluricentimetric to pluri-decimetric-large geodic cavities or centimetric veinlets. This geodic fluorite (Fl_{geo}) forms millimetric to centimetric well-developed white and yellow/honey translucent cubes which are more or less interlinked (Figure 3b). These crystals are fractured and contain many fluid inclusions (Figure 3c). Under cathodoluminescence, Fl_{geo} displays a light-blue luminescent core (Figure 3d).

Geodic fluorites (Fl_{geo}) sometimes display one or several overgrowths (Fl_{og}). It appears under cathodoluminescence as a dark-blue band at the extremity of the geodic crystals, with a thickness varying from 50 to 500 µm (Figure 3e). These overgrowths form the third and last stage of fluorite. They appear translucent in transmitted plane polarized light and do not contain any fluid inclusions (see Fig. A2 of Appendix A). From the center to the border, two growth phases have been noted (1) a translucent fluorite initiated by one or several purple rims ($Fl_{og}1$) (2) a second growth stage of fluorite with a laminar texture ($Fl_{og}2$), delineated by a fringe of well-aligned small globular pyrite crystals of about 30µm (Figure 3e and 3f). These pyrite crystals are rarely oxidized along fractures (Figure 3e).

Fission track mapping carried out on Fl_{geo} and $Fl_{og}1\&2$ shows that Fl_{geo} and $Fl_{og}1$ are almost devoid of tracks, while a high track density is observed in $Fl_{og}2$ (Figure 3g and 3h). Significant uranium content is thus measured only in $Fl_{og}2$, with U concentration varying from 5 to 58 ppm according to the track counting zones with an average from 9 to 30 ppm per sample (see Table A2 of Appendix A for details).

https://doi.org/10.5194/gchron-2020-33
Preprint. Discussion started: 24 November 2020

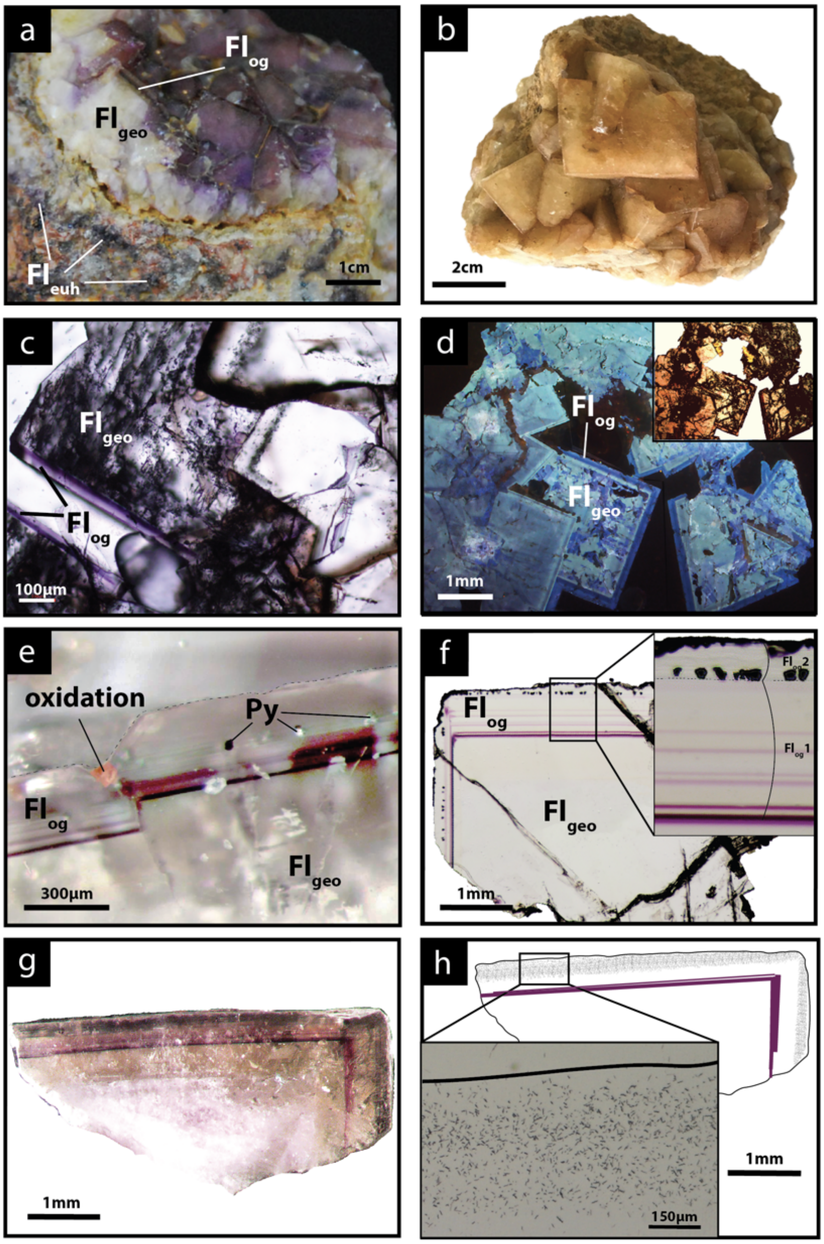

Figure 3: Photographs of the fluorite stages from the Pierre-Perthuis ore. (a) Geode in the altered granite with milky white cubic crystals (Fl$_{geo}$) and the translucent fluorite overgrowth (Fl$_{og}$) delimited by a thin purple band. The euhedral fluorite (Fl$_{euh}$) forms patches in the Avallon granite, from Gigoux et al., 2015 , (b) Centimetric cubes of Fl$_{geo}$, (c) Transmitted light microscopy photography of Fl$_{geo}$ and the overgrowth corresponding to Fl$_{og}$, (d) Cathodoluminescence image of Fl$_{geo}$ and Fl$_{og}$, (e) Photography of the limit between Fl$_{geo}$ and Fl$_{og}$ with a pyrite crystal affected by a fracture and oxidized, (f) Photography of a geodic fluorite crystal in transmitted light with the two stages constituting Fl$_{og}$ (1) a translucent fluorite initiated by one or several purple rims: Fl$_{og}$1; (2) a final growth stage of laminar fibrous fluorite with pyrite inclusions: Fl$_{og}$2, (g) Photography in transmitted light of an irradiated crystal of Fl$_{geo}$ + Fl$_{og}$, (h) Corresponding interpreted map of the induced fission tracks distribution in a crystal illustrated in (g) with a zooming on the muscovite detector.

4.2 Sulfur stable isotope composition

SIMS analyses were carried out for two fluorite crystals containing pyrite inclusions in their rims (Figure 4). Five pyrite crystals in PP18S3 sample have δ^{34}S values varying from –23.1 to –24.9 ‰$_{\text{V-CDT}}$. The sulfur isotopic ratio of pyrite from PP18S7 sample varies from –19.9 to –24.7 ‰$_{\text{V-CDT}}$. The mean of δ^{34}S values for PP18S3 and PP18S7 are –24.2 and –23.6 ‰$_{\text{V-CDT}}$, respectively. Two-sigma uncertainty is below 0.4 ‰$_{\text{V-CDT}}$.

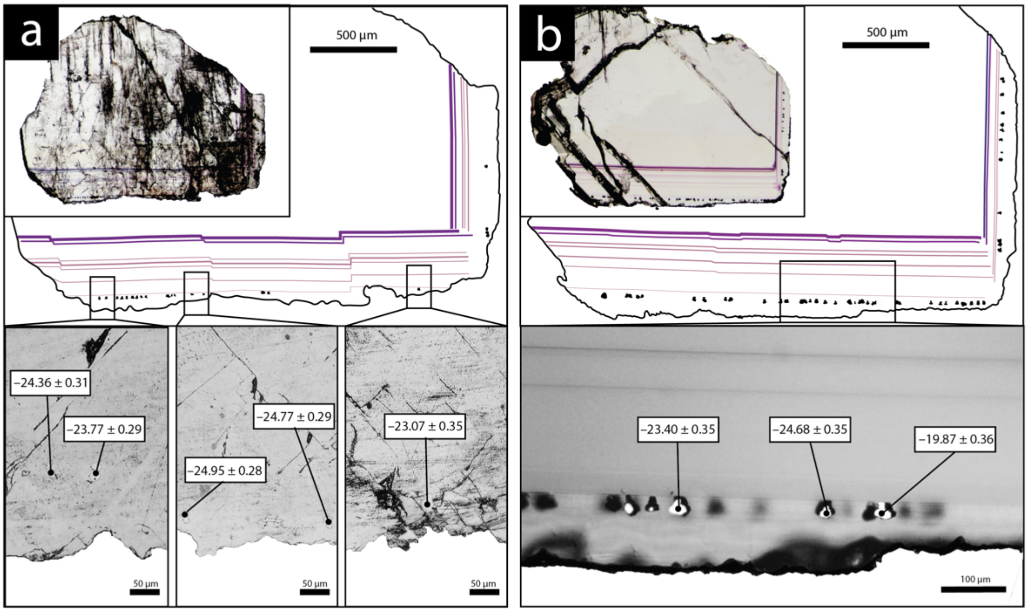

Figure 4: Location of SIMS spots for δ^{34}S measurements presented in ‰V-CDT for (a) sample PP18S3 and (b) sample PP18S7. Micro-photographs are in transmitted plane polarized light for the entire sample (upper left) and in reflected plane polarized light on gold metallized zoomed areas.

4.3 SR-XRF mapping

We studied in detail a sample that contains the last two generations of fluorite (Fl$_{\text{geo}}$ and Fl$_{\text{og}}$ described above) to investigate geochemical heterogeneities. Synchrotron radiation XRF mapping of a transect from Fl$_{\text{geo}}$ and Fl$_{\text{og}}$2 shows areas of lower concentration of Ca within the Fl$_{\text{og}}$2 exclusively, and higher concentrations of substituted elements such as Y, Sr, U and Pb (Figure 5).

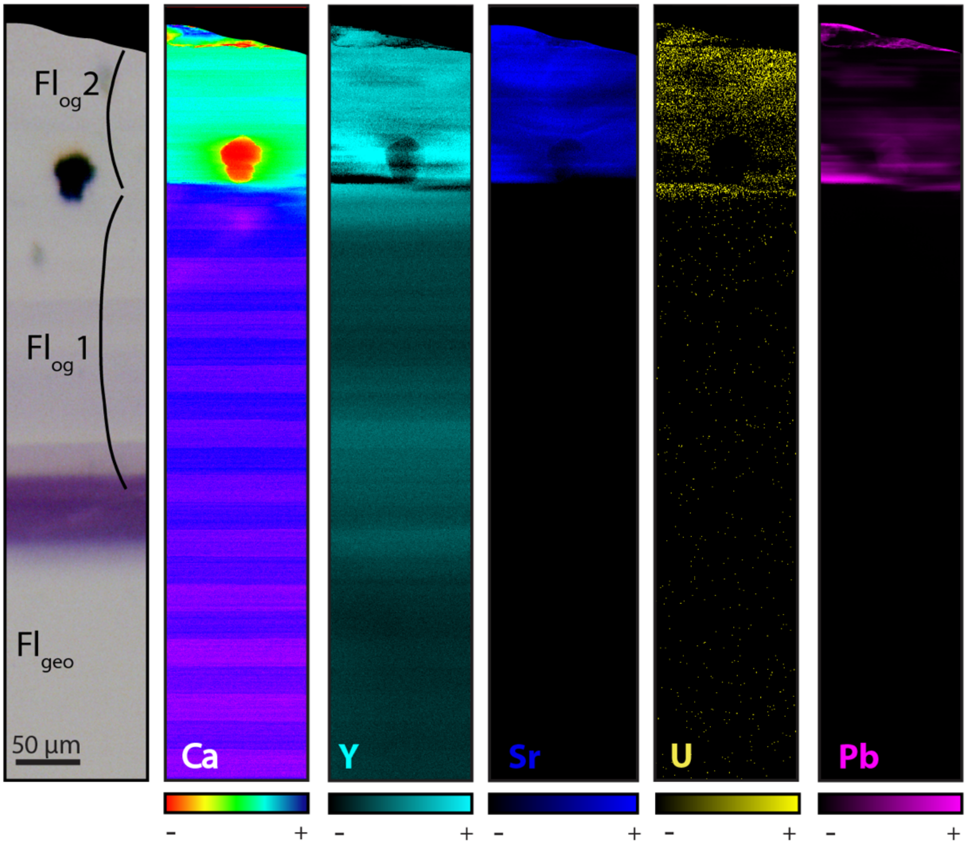

305

Figure 5: Transmitted plane polarized light photography from PP18S15 and corresponding Synchrotron radiation X-ray fluorescence elemental maps. Black areas indicate concentration below the limit of detection of the element. A globular pyrite crystal is included in $Fl_{og}2$.

310 Other maps have been generated with a focus on the transition between $Fl_{og}1$ and $Fl_{og}2$ (Figure 6), highlighted as distinct by petrographic observations and fission track mapping (Figure 3f and 3h). This map reveals elemental substitution and uranium incorporation. At this scale, SR-XRF mapping shows enrichment in Fe, Th, Sr, Pb, Y and U in $Fl_{og}2$. Th and Pb maps are highly correlated and show three growth bands anti-correlated with Y.

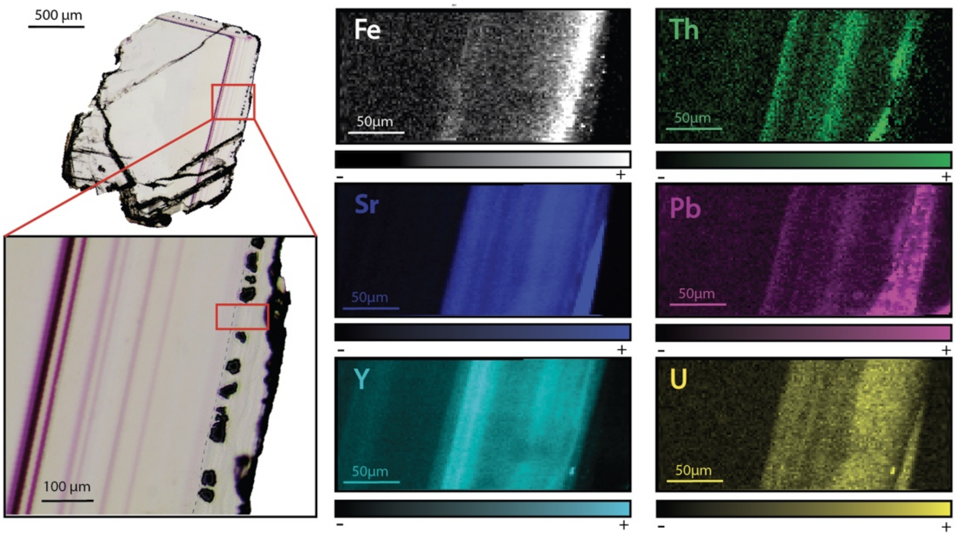

Figure 6: SR-XRF imaging of the transition between Fl$_{og}$1 and Fl$_{og}$2 in PP18S15 showing the distribution of Fe, Th, Sr, Pb, Y and U contents. Map dimensions are 261µm x 122µm.

4.4 U-Pb geochronology

Uranium and lead isotopic compositions are plotted in Tera-Wasserburg graphs ($^{238}U/^{206}Pb$ vs $^{207}Pb/^{206}Pb$) in Figure 7.

Four isochrons have been calculated, with a common initial $^{207}Pb/^{206}Pb$ composition ranging from 0.815 to 0.840. Outer rims of geodic fluorite crystals from Pierre-Perthuis yield an age of 38.7 ± 1.5 [1.8] Ma with 9 analyses and a MSWD of 0.68 (Figure 7a) for PPVi2, 41.1 ± 1.8 [2.2] Ma (MSWD = 1 and n=15) for PPVi5 (Figure 7b), 40.8 ± 3.0 [3.4] Ma for PP1802 with 11 analyses and a MSWD = 0.6 (Figure 7c) and PP15 of 41.8 ± 2.4 [2.8] Ma (MSWD=1.5 and n=22) (Figure 7d). As these ages are identical within analytical uncertainties, all data from the different crystals but corresponding to the same generation according to petrography, were then plotted in a single graph (Figure 7e), giving an age of 40.0 ± 0.9 [1.7] Ma (MSWD=1.2). Because U/Pb ratios are variable in the samples, data is well distributed in the Tera-Wasserburg space, and the isochron is rather well constrained despite the somehow large uncertainty of single analytical spots.

To evaluate the accuracy of fluorite LA-ICP-MS U-Pb dating in the absence of calibration against a fluorite primary RM, we tested the HK13 fluorite, a sample independently dated at 290 ± 10 Ma by (U–Th–Sm)/He thermochronology (Wolff et al., 2016). Although we found an age of 285.9 ± 30.9 Ma (Fig. A1 of Appendix A), interpretation of results is somehow limited by a poor data spread in a Tera-Wasserburg diagram and by rather large uncertainties regarding single analytical spots related to unstable ablation rates.

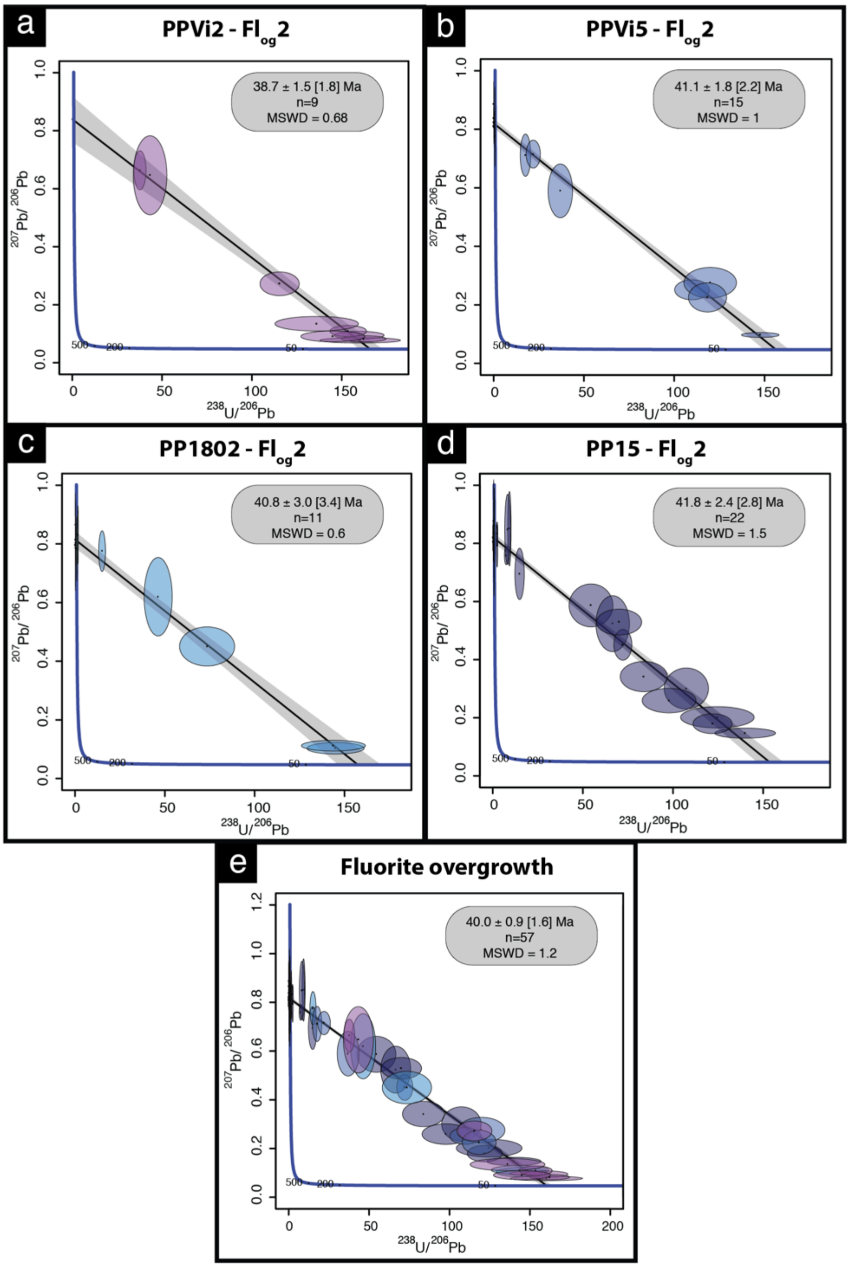

335 **Figure 7: Tera-Wasserburg diagram (^{207}Pb/^{206}Pb vs. ^{238}U/^{206}Pb) for fluorite. (a,b,c and d) U-Pb ages of the four fluorite overgrowth samples. (e) Isochron obtained from the compilation of all data illustrated in a,b,c and d. "n" is the number of analytical spots for each sample.**

5 Discussion

5.1 Uranium and lead incorporation in fluorite

The fluorite overgrowths are composed of two distinct layers: (1) $Fl_{og}1$, without significant integration of U in the fluorite lattice and (2) $Fl_{og}2$, in which U was effectively incorporated within the crystal and correlated with precipitation of pyrite. $Fl_{og}2$ appears colorless with an internal fibrous texture. No pleochroic halos were observed (Dill and Weber, 2010). Fission track mapping instead shows a homogeneous incorporation of U (Figure 3g and 3h). On a smaller scale, SR-XRF reveals micrometer-scale fluctuations in uranium concentrations along the growth directions, correlated with the incorporation of other substituted elements such as Sr and Zr (Figure 8).

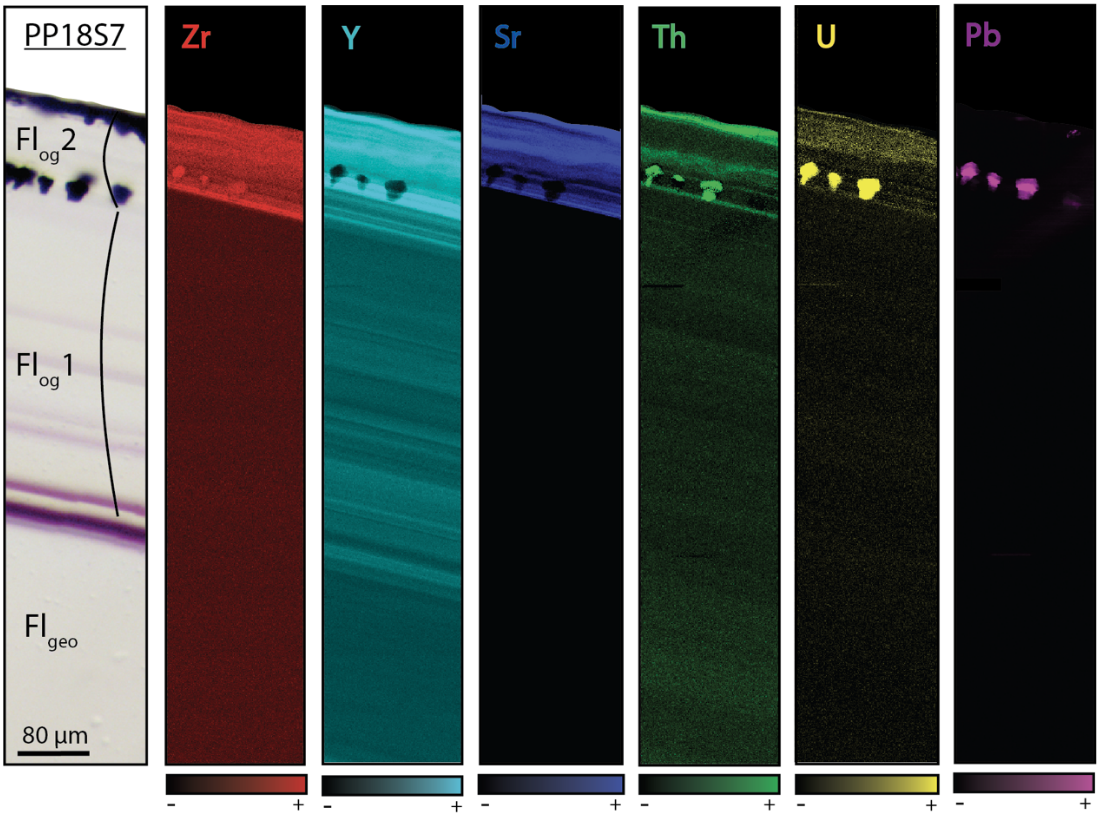

Figure 8: Synchrotron-based XRF elemental maps showing distribution of Zr, Y, Sr, Th, U and Pb through a transect from the core crystal of Fl_{geo} to the Fl_{og} rim of PP18S7. Color bars indicate intensity scale (black indicates concentrations below the detection limit). Higher intensities correspond to higher metal contents. Map dimensions are 179µm x 1mm.

The transition between Fl$_{og}$1 and Fl$_{og}$2 can be explained by the development of a redox front, causing the reduction of U$^{(VI)}$ into U$^{(IV)}$. Theoretically, fluorite can incorporate U$^{(IV)}$ as UO_2 and U$^{(VI)}$ as $CaUO_4$ (Kröger, 1948; Recker, 1961). Recently, reported hexavalent uranium in fluorite from the Round Top Mountain in Texas (USA). In Pierre-Perthuis, the presence of numerous pyrite crystals in Fl$_{og}$2, similar to those reported by Dill and Weber (2010), characterizes a reducing environment that has probably initiated the precipitation of U. Pyrite is common in roll-front uranium deposits (Bonnetti et al., 2015; Cai et al., 2007; Campbell et al., 2012; Ingham et al., 2014). Globular pyrites, similar to those observed in Fl$_{og}$2, are usually interpreted as biogenic in origin This hypothesis is supported by the sulfur stable isotope composition of the pyrites included in Fl$_{og}$2 (mean $\delta^{34}S = -23.6$ ‰$_{V\text{-}CDT}$) (Belyi et al., 1972; Blakeman et al., 2002; Chen et al., 2019; Bonnetti et al., 2020; Cai et al., 2007; Rackley, 1972). The homogeneous $\delta^{34}S$ of these pyrites indicates a large amount of sulfate available for reduction by bacteria in an open system (Hough et al., 2019; Magnall et al., 2016). Concentric incorporation of Ni, As, and Cu were reported both in biogenic (Baumgartner et al., 2020) and abiogenic pyrite (Wu et al., 2019). Pyrite crystals in Fl$_{og}$2 show such concentric zonation (Figure 9).

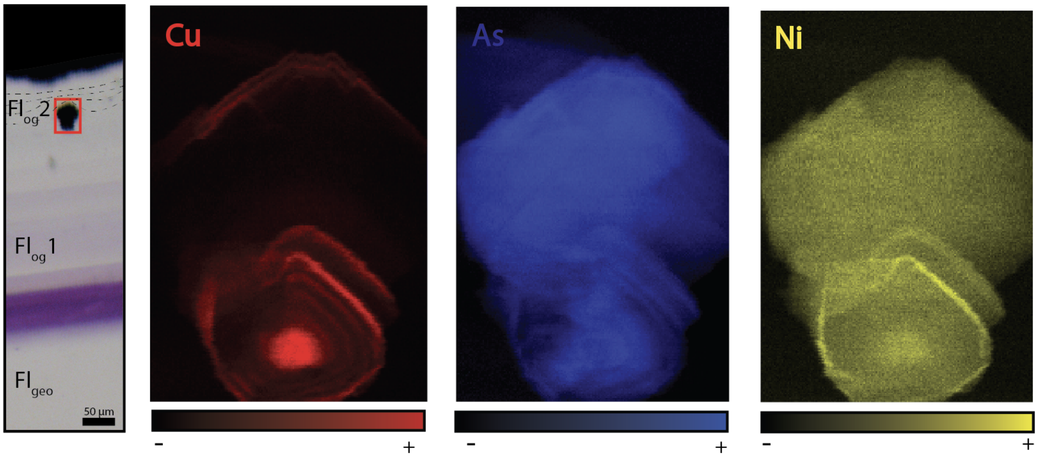

Figure 9: Copper, arsenic and nickel distribution maps of a pyrite included in Fl$_{og}$2. Maps dimensions are 52 µm x 76 µm.

Hence, we propose that uranium incorporation in Fl$_{og}$2 is related to BSR (Figure 10). The solubility of uranium was enhanced by F-bearing solutions (Xing et al., 2019) that leached the granitic basement through the fracture network (Figure 10 a). When reaching the unconformity between the basement and the sedimentary cover, a local redox front generated by BSR causes U to precipitate. BSR produces sulfur species reacting with iron oxyhydroxides or dissolved iron to form iron disulphides (Bonnetti et al., 2017; Machel, 2001). These sulfur species are electron donors that can reduce U$^{(VI)}$ to insoluble U$^{(IV)}$, thus causing uranium precipitation (Bonnetti et al., 2015; Campbell et al., 2012; Yi et al., 2007). Alternatively, direct microbial reduction of U could also have occurred (Bhattacharyya et al., 2017; Lovley et al., 1991). The incorporation of U, together with other metals (Figure 5 and 6), may have been enhanced through their adsorption by bacterial bio-films developed at the surface of fluorite crystals. Indeed, the collomorphic fibrous texture of the external overgrowth $Fl_{og}2$ in the Pierre-Perthuis crystals (Figure 3f) could result from the development of bio-films in pore/geode linings. Although the secretion of extracellular polymeric substances leading to the formation of bacterial bio-films on pyrite has been extensively documented, their development at the surface of fluorite crystals remains largely unexplored, apart from Heim et al., (2012) who reported tubular structures within fluorite filling fractures in the Äspö diorite in Sweden, interpreted as fossilized microbial bio-films.

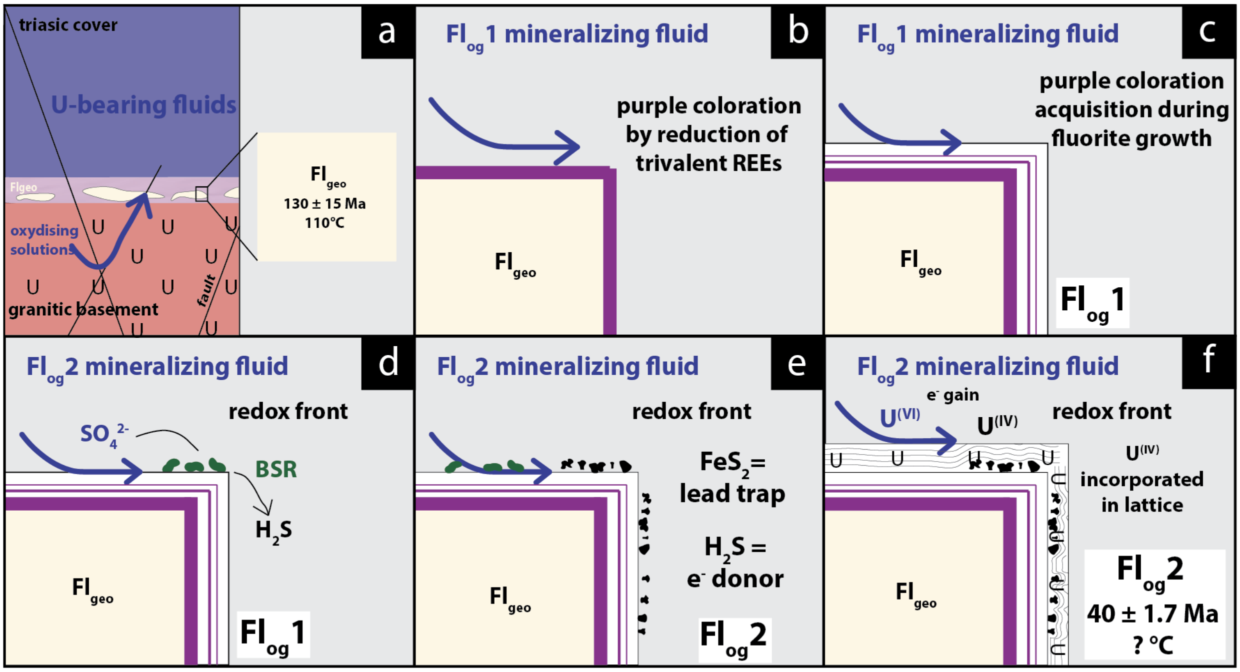

Figure 10: Conceptual model of uranium incorporation in the fluorite lattice. a) Uranium is leached by F-rich oxidizing solutions flowing through the granitic basement and reaching Fl_{geo} in the basement/cover interface, b) formation of purple layers on the fluorite surface by F-bearing fluids, c) Crystallization of $Fl_{og}1$, d) A local redox front is generated by BSR, e) sulfur species react with iron oxyhydroxides or dissolved Fe to form pyrite, f) reduced uranium is incorporated in $Fl_{og}2$.

The development of purple colorations in fluorite has long been recognized to be related to the vicinity of uranium-bearing minerals (Chatagnon et al., 1982; Pi et al., 2007). Bill and Calas (1978) proposed that the incorporation of Eu^{2+}, together with metallic calcium colloids formed by long-time irradiation, can cause purple colorations. Chatagnon et al., (1982) and later Kempe et al. (2002) show that such colorations have rather been caused by the reduction and stabilization of Tm and Ho in the divalent state under irradiation by the radioactive decay series of U. SR-XRF mapping focused on small well-defined purple growth bands (Figure 11) shows enrichment in U and Th. As the thickness of these bands is sometimes less than 10 µm, we suggest that the coloration was acquired through gamma irradiation, instead of α-irradiation, which would have caused larger bands (Dill and Weber, 2010; Pi et al., 2007; Vochten et al., 1977). It must be noted however that such coloration is not developed in the U-bearing $\mathrm{Fl_{og}2}$ layer (Figure 6, 8). Thus, the origin of the purple coloration in the fluorite 395 crystals of Pierre-Perthuis is still not fully understood and would require further investigation.

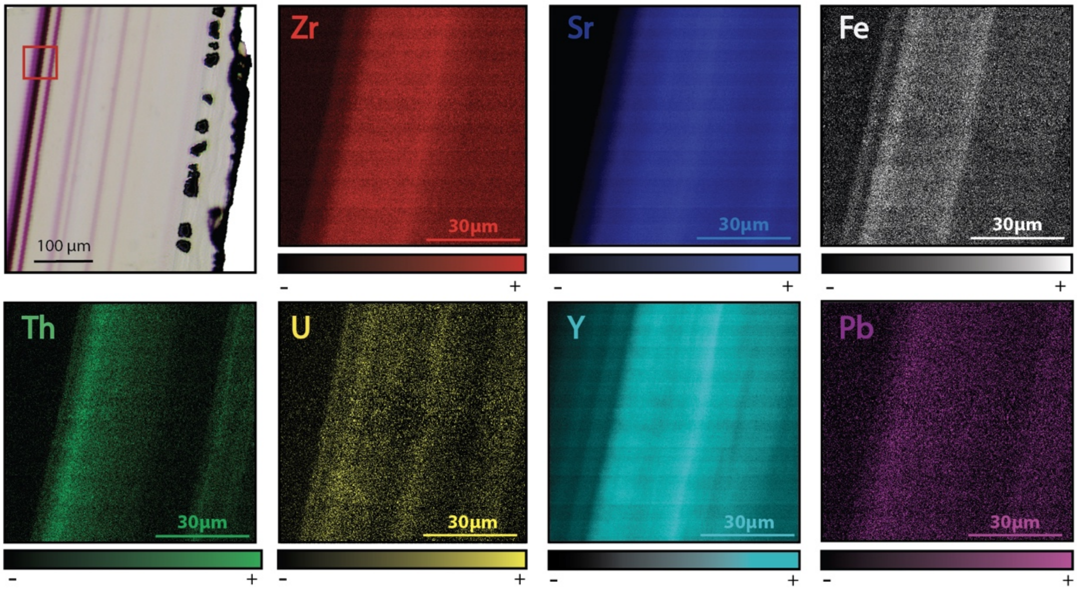

Figure 11: Transmitted plane polarized light photography from PP18S7 and corresponding Synchrotron X-ray fluorescence elemental maps. Area of XRF scan is outlined by a red box on the photography. Map dimensions are 80 x 80 µm.

400 Lead was detected by SR-XRF mapping, and its distribution in $\mathrm{Fl_{og}2}$ seems to be correlated with Th (Figure 6 and 11). During the co-precipitation of pyrite and $\mathrm{Fl_{og}2}$, lead was preferentially incorporated into pyrite crystals (Figure 8).

In the following section, we will further discuss the spatial distribution and retention of U and Pb and the reliability of the U-Pb geochronometer in fluorite.

5.2 Fluorite U-Pb geochronology

405 5.2.1 Retention of U in fluorite

To test the reliability of U-Pb dating in the fluorite rims of Pierre-Perthuis, we further discuss potential alterations by (1) the development of fractures and cleavages; (2) dissolution and re-crystallization; (3) solid-state diffusion.

(1) Fractures and cleavages

https://doi.org/10.5194/gchron-2020-33
Preprint. Discussion started: 24 November 2020

Fluorite is well known to develop cleavages and fractures. Although cleavages are abundant in the core of the crystals (Fl_{geo}), they are rare on the rims (Figure 3c). Scarce fractures crosscutting $Fl_{og}2$ were observed, causing the oxidation of pyrite (Figure 3e). Adjacent pyrite crystals being unaffected, these fractures only generated local alterations, and were consequently avoided in LA-ICP-MS analyses (Figure 3e).

(2) Dissolution-re-crystallization

Dissolution and re-precipitation of fluorite in hydrothermal deposits is common (Burisch et al., 2017). In Pierre-Perthuis, some crystals show irregular extremities demonstrating that a late fluid event was able to slightly dissolve fluorite. These corroded crystals were not selected for LA-ICP-MS analyses. In the other crystals, the preservation of pyrite crystals, the internal fibrous texture of fluorite and the perfect geometric relationship between Fl_{geo} and Fl_{og} (Figure 3f) demonstrate that $Fl_{og}2$ was not dissolved and re-crystallized.

(3) Solid-state diffusion

Cherniak et al., (2001) determined the diffusion rates of Sr, Y, and REE in natural fluorite and concluded that no significant diffusion (< 100 µm) should occur at temperatures below 500 °C. Bosze and Rakovan, (2002), however, document diffuse boundaries between REE sectoral zoning in fluorite, interpreted as resulting from the diffusion of these elements over an area of 200 - 300 µm. In Pierre-Perthuis, the preservation of ca. 10 µm thick violet bands with sharp terminations demonstrates the absence of significant REE diffusion (Kempe et al., 2002). SR-XRF mapping also shows the preservation of Sr, Y, Th, Pb and U-rich bands of a thickness of ca. 10µm (Figure 6), evidencing the absence of solid-state diffusion of these elements in our samples. Although the crystallization temperature of $Fl_{og}2$ is unknown due to the absence of fluid inclusions, a maximum temperature of 100 °C is speculated based (1) on the fluid inclusion homogenization temperature ranging from 80 to 100°C for Fl_{geo} at Pierre-Perthuis (Gigoux et al., 2016), (2) on evidence of BSR and (3) on the fact that the paleotemperatures reached by the *Assise de Chitry* Fm in the area were low during the Cenozoic period (Barbarand et al., 2013; Gigoux et al., 2016). We thus conclude that U and Pb did not diffuse within $Fl_{og}2$.

5.2.2 In situ LA-ICP-MS U-Pb dating

Uranium concentration in fluorite is highly variable (Piccione et al., 2019; Walter et al., 2018; Wolff et al., 2016), and is often insufficient for U-Pb dating (Piccione et al., 2019). In the Pierre-Perthuis fluorite ore, the geodic fluorite Fl_{geo}, dated at 130 ± 15 Ma by Sm-Nd (Gigoux et al., 2015), could not have been tested for U-Pb geochronology because it contains no U. Likewise, $Fl_{og}1$ is not amenable to U-Pb dating. The first fluorite generation, Fl_{euh}, precipitated from the dissolution of the host dolomite rock, and therefore contains too many carbonate impurities that cannot be excluded from sampling in LA-ICP-MS.

Compared to U-Pb geochronology of other common lead-bearing minerals such as calcite (e.g., Roberts et al., 2020), fluorite U-Pb geochronology presents some additional analytical challenges. Laser induced damages in fluorite have been extensively studied (De Bonis et al., 2014; Jia et al., 2005; Rafique et al., 2012; Reichling et al., 1994). Due to thermal stress and shock waves, large fractures and the ejection of solid fragments commonly occur during the first laser shots (Gogoll et al., 1996; Johansen et al., 1995). A 7s pre-ablation, excluded from data used for U-Pb age calculation, helps in getting more stable ablation rates.

Ablation quality depends on numerous factors including laser parameters (wavelength, fluence and repetition rate) and intrinsic crystallographic features like orientation, chemical impurities or defects (Gogoll et al., 1996). Therefore, ablation rate and quality may largely vary from one natural fluorite crystal to another.

Variations in ablation rates (crater depth/crater diameter) may generate variable downhole fractionations (DF). To minimize DF, a low laser fluence (typically 1J.cm^{-2}) and a large diameter are generally preferred (Mangenot et al., 2018). However, a fluence of at least 6J.cm^{-2} was required to ablate Fl$_{og}$2. SEM observations of ablation pits in Fl$_{og}$2 reveal variable laser crater aspect ratios (see Fig. A3 of Appendix A for spots illustration and measured crater depths). The total crater depths, including the material excluded for analysis during the 7s "pre-ablation" vary from 97 to 153 µm in Pierre-Perthuis fluorite samples and from 231 to 266 µm for the HK13 fluorite (see Table A3 of Appendix A). To correct for DF, a matrix-match primary RM can be used if laser ablation generates similar crater aspect ratios between the reference material and unknown samples (Elisha et al., 2020; Guillong et al., 2020). Such a matrix-match RM is not yet available for fluorite U-Pb geochronology (Piccione et al., 2019). However, even with the use of such a RM, DF correction may turn out to be incorrect because of variable crater aspect ratios in fluorite. Further research is needed to improve the precision and accuracy of fluorite U-Pb geochronology, through the systematic comparison of LA-ICP-MS crater aspect ratios in fluorite samples of known ages. In addition to DF, other sources of elemental fractionation should also be investigated, such as the influence of the chemical composition of the aerosol (Sylvester, 2008). Piccione et al. (2019) reported comparable U-Pb ages acquired on fluorite and associated nacrite, suggesting that this effect may not introduce a significant bias.

5.3 U-Pb age significance

In the absence of elemental fractionation correction against a fluorite RM, the age of the last generation of fluorite in Pierre-Perthuis ore (Fl$_{og}$2), 40.0 ± 1.7 Ma, may be over- or underestimated. Considering an age offset of 20% as an extreme case (Guillong et al., 2020), this age estimate still significantly differs from the Sm-Nd age of 130 ± 15 Ma (Gigoux et al., 2015) of the prior geodic fluorite crystals Fl$_{geo}$.

5.3.1 Regional significance

Bergerat, (1984) proposed an N-S compressive stress field during the Eocene through micro-structural analysis in the studied area, interpreted as the consequence of the Pyrenean compression. Evidence of late Eocene fragile deformation and associated fluid flows are also found in the eastern Paris basin, ca. 150 km north-east of Pierre-Perthuis, where calcite cementing hydraulic breccia were dated at 43 ± 1 Ma (Brigaud et al., 2020; Pagel et al., 2018). Volcanic activity in the northern part of the French Massif Central has been reported by Bellon et al., (1974) and Lefort and Agarwal, (2002) during this period, at about 80-120km south-east of the study area. In conclusion, a local compressive stress field related to the propagation of N-S Pyrenean compression in the intraplate domain may have generated fluid flows and the crystallization of $Fl_{og}2$.

5.3.2 Wider considerations regarding radiometric dating of ore deposits

In Pierre-Perthuis, the geodic fluorite crystals Fl_{geo} yield a Sm-Nd age of 130 ± 15 Ma (Gigoux et al., 2015). Here, we show that later fluid flows took place during the Cenozoic period, recorded as rims overlaying Fl_{geo}. Hence, successive mineralizing fluids occur during a time period of ca. 90 Ma.

In some ore deposits, fluorite Sm-Nd dating is the only available geochronometer. However, errorchrons and imprecise ages may occur. In such cases, U-Pb geochronology of common lead-bearing authigenic phases such as calcite (Rasbury and Cole, 2009), hematite (Walter et al., 2018), chalcedony (Nuriel et al., 2011) or nacrite (Piccione et al., 2019) offers new perspectives to gain knowledge on the successive chronology of mineralizing fluid flows. In Pierre-Perthuis however, as in some other F-Ba deposits, these minerals are absent. A late Eocene age estimate for the last fluorite-mineralizing event reveals that the "lifetime" of the ore deposit was much longer than previously thought. Fluorite was deposited during several successive fluid flows induced by the reactivation of faults affecting the granitic basement. Small-scale radiometric dating of single growth bands in authigenic phases makes it possible to determine the chronology of these multiple crystallization events. Future research should be conducted to test the U-Pb geochronometer in fluorite crystals dated by Sm-Nd or other direct ((U–Th–Sm)/He) or indirect methods.

6 Conclusion

We have explored the U-Pb geochronometer in fluorite. In the Pierre-Perthuis F-Ba deposit, uranium was found in the most external rim of fluorite crystals. SR-XRF mapping demonstrates the preservation and retention of micrometer-thick zonation in uranium concentration in fluorite. Petrographic observations coupled to induced fission tracks and SR-XRF mapping show that uranium is incorporated in the fluorite crystal lattice by elemental substitution. The incorporation of uranium is related to bacterial sulphate reduction, evidenced by globular pyrite inclusions. Relying on careful and detailed petrography, we show that such growth bands can be dated by U-Pb geochronology. The spread of U and Pb isotopic compositions in a Tera-Wasserburg space are interpreted as isochrons, yielding an age of 40.0 ± 1.7 Ma, not corrected for matrix-related elemental fractionation. This age estimate corresponds to the last minor fluorite-mineralizing event. Since the crystal cores were previously dated at 130 ± 15 Ma by Sm-Nd, successive episodic fluid flows occurred during ca. 90 Ma. Future research should be conducted to correct for $^{238}U/^{206}Pb$ fractionation during LA-ICP-MS analysis in fluorite through the definition of a fluorite reference material. 500

Appendix A

Laboratory and Sample Preparation	
Laboratory name	Géosciences Paris Sud (GEOPS). Université Paris-Saclay. Orsay. France
Sample type/mineral	Fluorite
Sample preparation	Fluorite crystals mounted in epoxy resin
Imaging	Optical microscopy using transmitted light
Laser ablation system	
Make. Model and type	193nm ArF (Teledyne Photon Machines)
Ablation cell	HelEx
Laser wavelength (nm)	193 m
Pulse width (ns)	5 ns
Fluence (J.cm-2)	6.25 $J.cm^{-2}$
Repetition rate (Hz)	10 Hz
Pre-ablation	each spot during 7 s
Ablation duration (secs)	30 s
Spot size (mm)	150 µm
Sampling mode / pattern	Static spot ablation
Carrier gas	He
Cell carrier gas flow ($l.min^{-1}$)	Helium Lage volume : 0.5 $l.min^{-1}$ Inner cup : 0.375 $l.min^{-1}$
ICPMS instrument	
ICPMS instrument Make. Model & type	ThermoScientific Element XR
Sample introduction	Ablation aerosol
RF power (W)	1175 W
Make-up gas flow in ablation funnel ($l.min^{-1}$)	Ar=0.950 to 1 $l.min^{-1}$
Detection system	Ion counter
Masses measured	206. 207. 208. 232. 238

Average gas background (cps) 2019-12-19	12 for 206. 10 for 207. 26 for 208. 0.1 for 232. 0 for 238
Average gas background (cps) 2019-12-20	20 for 206. 17 for 207. 53 for 208. 0.1 for 232. 0 for 238
Integration time per peak (ms)	10 ms for ^{208}Pb. ^{232}Th. ^{238}U. of 30 ms for ^{206}Pb and of 40 ms for ^{207}Pb by 70 runs
Total integration time per reading (secs)	0.1 s
IC Dead time (ns)	30 ns
Signal strength at ICPMS tuned conditions	Th/U=1.02 248ThO/232Th below 0.3%
Data Processing	
Data acquisition	Fully automated mode overnight in sequences of 399 analysis maximum
Gas blank	30 s background. 30 s sample ablation and 30 s washout
Calibration strategy	NIST614 for Pb-Pb. calcite WC-1 for U-Pb. secondary reference materials: calcite Duff Brown Tank (DBT). calcite breccia AUG-B6 and fluorite HK13
Reference Material info	WC-1 age: 254.4±6.4 Ma (Roberts et al., 2017). Duff Brown Tank age: 64±0.7 Ma (Hill et al., 2016). Calcite breccia AUG-B6 age: 43±1 Ma (Pagel et al., 2018) and fluorite HK13 age: 290±10 Ma (Wolff et al., 2016)
Data processing package used / Correction for LIEF	Iolite to calculate uncertainties. no down-hole fractionation correction
Mass discrimination	^{207}Pb/^{206}Pb normalization to NIST614. ^{206}Pb/^{238}U normalization to WC-1
Common-Pb correction. composition and uncertainty	No common-Pb correction applied
Uncertainty level & propagation	Ages in the data table are quoted at 2sigma (2σ) absolute. uncertainty propagation by quadratic addition
Quality control / Validation 2019-12-19	Measurements of WC-1 age = 167.7 ± 3.5 Ma. Duff Brown Tank (DBT) age = 63.75 ± 2.03 Ma. AUG-B6 age = 40.7± 1.61 Ma and NIST614 were done along with samples throughout the analytical session
Quality control / Validation 2019-12-20	Measurements of WC-1 age = 148.9 ± 2.2 Ma. Duff Brown Tank (DBT) age = 64.57 ± 2.95 Ma. AUG-B6 age = 44.45 ± 2.17 Ma. “HK13” fluorite was dated at 290.38 ± 14.38 [17.52] Ma and NIST614 were done along with samples throughout the analytical session

Table A1: Data for fluorite LA-ICP-MS U-Pb analysis at University Paris-Saclay, GEOPS laboratory.

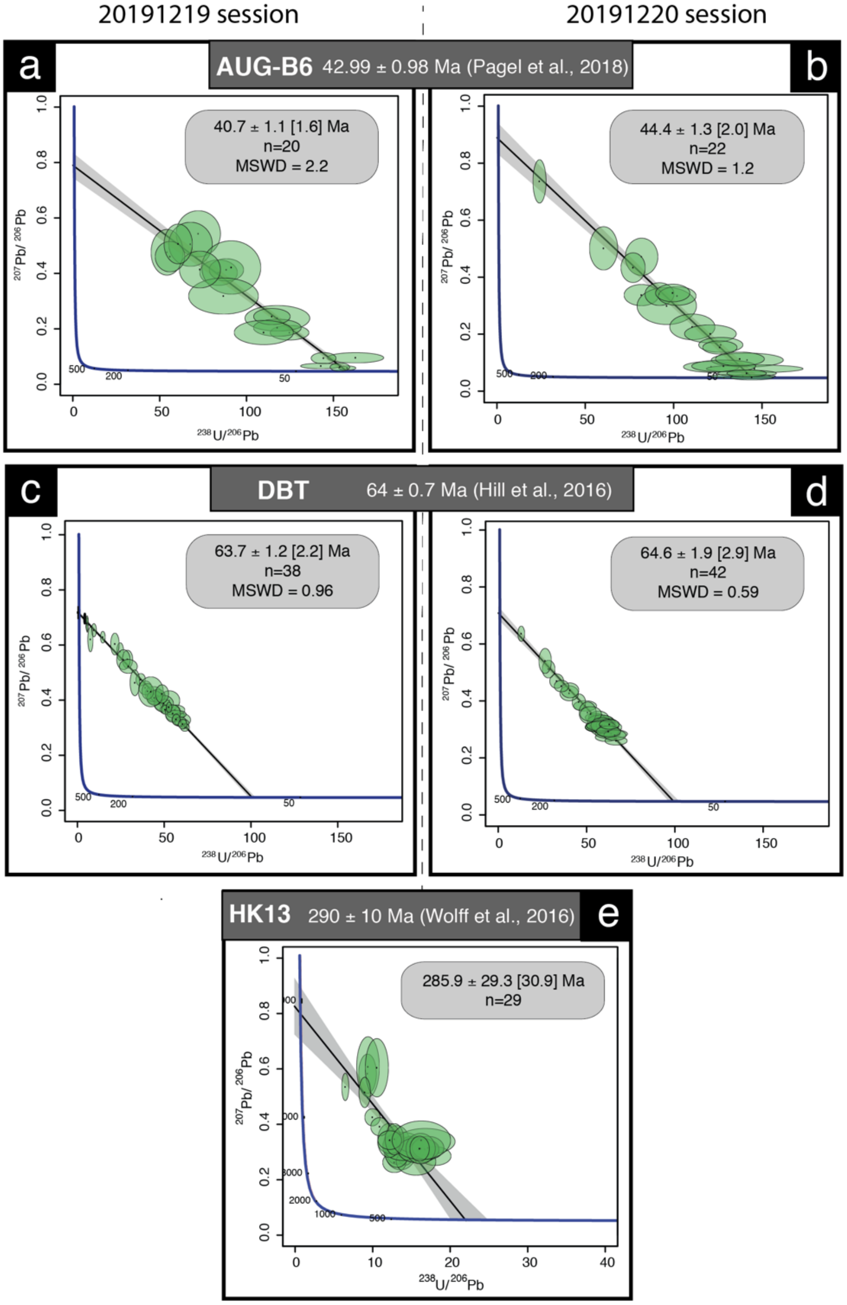

Figure A1: Tera-Wasserburg diagrams of primary and secondary calcite and fluorite reference materials and measured during analytical sessions. (a,b) Tera-Wasserburg diagrams displaying corrected ages for the calcite Breccia of the Gondrecourt graben AUG-B6 measured during the two analytical sessions, (c,d) Tera-Wasserburg diagram displaying the Duff Brown Tank corrected ages measured during the two analytical sessions, (e) Tera-Wasserburg diagram of "HK13" fluorite dated at 290 ± 10 Ma by Wolff et al., 2016.

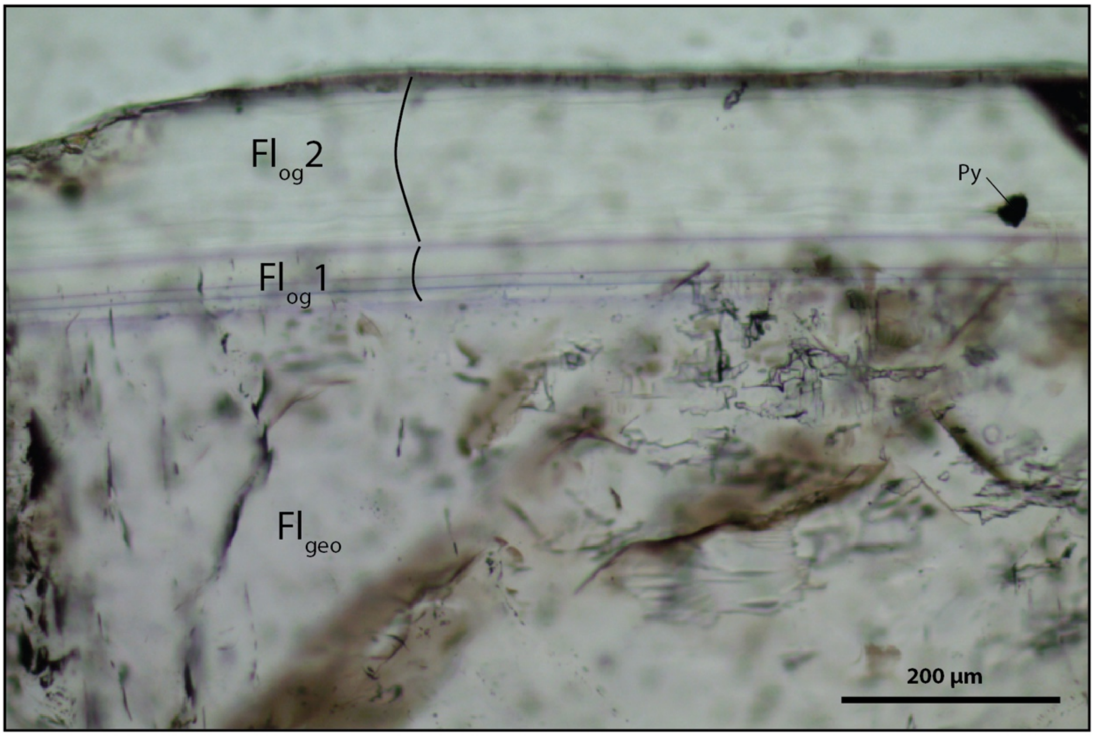

510

Figure A2: Photography of the fluorite stages from the Pierre-Perthuis ore showing the contrast in fluid inclusions concentration between Fl$_{geo}$ and Fl$_{og}$.

Sample	zone	counted fission tracks	area (μm^2)	U concentration (ppm)	U average concentration /sample (ppm)
CORNING CN5	-	131	10^4	12.17	-
PP1802-1	1	57	3000	18	19
	2	57		18	
	3	54		17	
	4	63		20	
	5	62		20	
	6	58		19	
	7	52		17	

	8	60		19	
PP1802-2	1	67	2500	26	29
	2	70		27	
	3	76		30	
	4	85		33	
	5	76		30	
PP1802-4	1	56	1500	38	30
	1 (rim)	22		15	
	2	58		39	
	2 (rim)	31		21	
	3	47		32	
	3 (rim)	25		17	
	4	86		58	
	4 (rim)	22		15	
	5	63		43	
	5 (rim)	29		20	
PP1801-2	1	36	3000	13	9
	2	28		10	
	3	26		9	
	4	13		5	
	5	22		8	
	6	25		9	
	7	33		11	
	8	13		5	
CORNING CN5	-	94	10^4	12.17	-

Table A2: Fission tracks analytical results. Counted areas are distributed along $\mathrm{Fl_{og}}2$ on different samples. Correcting factor employed for U concentration calculation on each sample depends on the counted area and followed a bracketing method (thanks to the two CN5 standard certified at 12.17ppm).

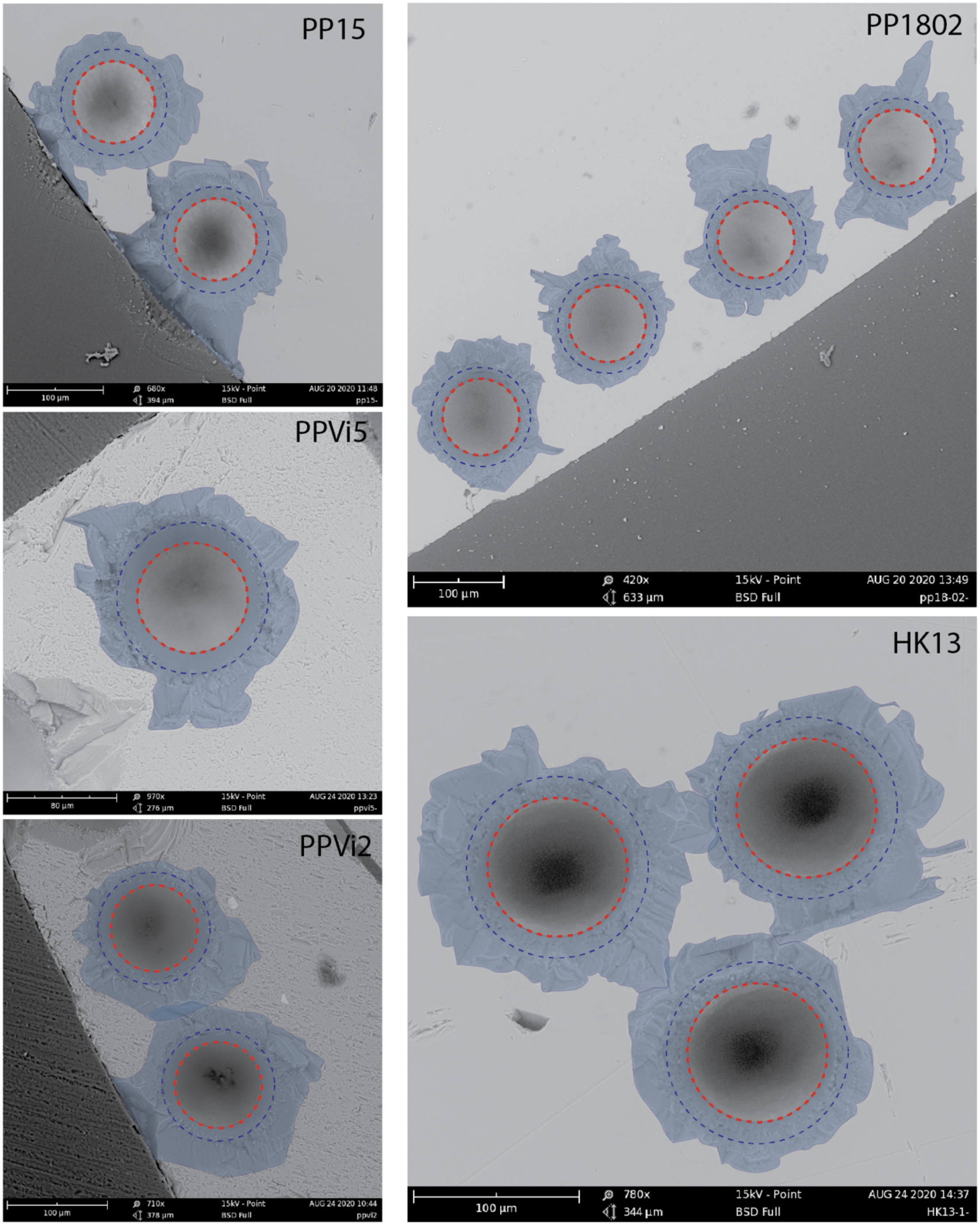

Figure A3: Various crater aspects induced by laser ablation on different fluorite sample imaged by Scanning Electron Microscopy. Blue circle shows the pre-ablation laser diameter (110 µm) and the red one the ablation laser diameter (85 µm).

Sample	**crystal**	**spot**	**distance to the source (µm)**		**crater depth**	**Average**
			surface of the sample	**bottom of the crater**	**(µm)**	**(µm)**
PP15	1	1	4244	4357	113	111
		2	4216	4336	120	
		3	4214	4312	98	
	2	1	4169	4276	107	
		2	4161	4287	126	
		3	4144	4261	117	
		24	4154	4251	97	
PP1802	1	1	4317	4444	127	112
		6	4255	4356	101	
		7	4230	4349	119	
		8	4192	4293	101	
PPVI2	1	3	4020	4164	144	133
		4	3982	4135	153	
		8	3977	4104	127	
		12	3957	4094	137	
		13	3950	4096	146	
		20	3889	4011	122	
		22	3869	3982	113	
		25	3882	4006	124	
PPVI5	1	2	4109	4234	125	138
		5	4080	4210	130	
		8	4082	4226	144	
		10	4047	4199	152	
HK13	1	1	4486	4730	244	249
		4	4478	4744	266	
		6	4457	4690	233	

2	2	4526	4757	231
	5	4540	4807	267
3	2	4496	4752	256
	4	4503	4752	249
4	2	4407	4646	239
	4	4430	4689	259

Table A3: Statistical analysis of crater depths induced by laser ablation for U-Pb dating by scanning electron microscopy. The crater depth includes the 7s pre-ablation.

Author contribution

Julius Nouet and Claire Boukari were involved in the preparation of the fluorite samples for SEM observations, SR-XRF $and induced fission track mapping. Andréa Somogyi directed the elemental mapping experiments on the Nanoscopium beamline at Synchrotron SOLEIL, and supervised SR-XRF data interpretation. Jocelyn Barbarand, Benjamin Brigaud and Maurice Pagel were involved in field work, data interpretation and contributed to the improvement of the manuscript. Louise Lenoir and Thomas Blaise participated in every step of the study and prepared the manuscript.

Competing interests

The authors declare that they have no conflict of interest.

Acknowledgments

The authors would like to thank Kadda Medjoubi for support and the scientific discussions during SR-XRF experiments on the Nanoscopium beamline at SOLEIL. We acknowledge Nordine Bouden and Johan Villeneuve for the acquisition of sulfur stable isotope ratios by SIMS at the CRPG. We would like to thank Frederic Haurine for his assistance during the acquisition of the U-Pb analyzes, performed on the LA-ICP-MS which is part of the PANOPLY platform (GEOPS-LSCE). Portions of this research were carried out at the SOLEIL Synchrotron Radiation Laboratory, a national user facility operated by CEA and CNRS (Proposal number: 20190188). This research was partly funded by TelluS Program CESSUR "*Connaissance et Technologie du Sous-Sol pour son Exploitation et Usage Durable*" of CNRS/INSU. Reinhard Wolff is warmly thanked for the sharing of fluorite sample HK13.

References

Alexandre, P., Kyser, K., Thomas, D., Polito, P. and Marlat, J.: Geochronology of unconformity-related uranium deposits in the Athabasca Basin, Saskatchewan, Canada and their integration in the evolution of the basin, Mineralium Deposita, 44(1), 41–59, doi:10.1007/s00126-007-0153-3, 2009.

Baele, J.-M., Monin, L., Navez, J. and André, L.: Systematic REE Partitioning in Cubo-Dodecahedral Fluorite from Belgium Revealed by Cathodoluminescence Spectral Imaging and Laser Ablation-ICP-MS, Proceedings of the 10th International Congress for Applied Mineralogy (ICAM), 23–30, doi:10.1007/978-3-642-27682-8_4, 2012.

Barbarand, J., Quesnel, F. and Pagel, M.: Lower Paleogene denudation of Upper Cretaceous cover of the Morvan Massif and southeastern Paris Basin (France) revealed by AFT thermochronology and constrained by stratigraphy and paleosurfaces, Tectonophysics, 608, 1310–1327, doi:10.1016/j.tecto.2013.06.011, 2013.

Baumgartner, R. J., Van Kranendonk, M. J., Pagès, A., Fiorentini, M. L., Wacey, D. and Ryan, C.: Accumulation of transition metals and metalloids in sulfidized stromatolites of the 3.48 billion–year–old Dresser Formation, Pilbara Craton, Precambrian Research, 337, 105534, doi:10.1016/j.precamres.2019.105534, 2020.

Bellon, H., Gillot, P. Y. and Nativel, P.: Eocene volcanic activity in Bourgogne, Charollais, Massif Central (France), Earth and Planetary Science Letters, 23(1), 53–58, doi:10.1016/0012-821X(74)90029-6, 1974.

Belyi, V., Vinogradov, V. and Lisitsin, A.: Sulfur isotope composition of uranium roll ore bodies and its genetic significance, Litologiya i Poleznye Iskopaemye, 6, 42–53, 1972.

Bergamaschi, A., Medjoubi, K., Messaoudi, C., Marco, S. and Somogyi, A.: MMX-I: A data-processing software for multi-modal X-ray imaging and tomography, Journal of Physics: Conference Series, 849, 012060, doi:10.1088/1742-6596/849/1/012060, 2017.

Bergerat, F.: La fracturation nivernaise : Influences bourguignonne et centralienne sur la structuration du Nivernais, Bulletin d'information des géologues du bassin de paris, 21(4), 27–31, 1984.

Bhattacharyya, A., Campbell, K. M., Kelly, S. D., Roebbert, Y., Weyer, S., Bernier-Latmani, R. and Borch, T.: Biogenic non-crystalline U(IV) revealed as major component in uranium ore deposits, Nature Communications, 8(1), 1–8, doi:10.1038/ncomms15538, 2017.

Bill, H. and Calas, G.: Color centers, associated rare-earth ions and the origin of coloration in natural fluorites, Physics and Chemistry of Minerals, 3(2), 117–131, doi:10.1007/BF00308116, 1978.

Blakeman, R. J., Ashton, J. H., Boyce, A. J., Fallick, A. E. and Russell, M. J.: Timing of Interplay between Hydrothermal and Surface Fluids in the Navan Zn + Pb Orebody, Ireland: Evidence from Metal Distribution Trends, Mineral Textures, and 34S Analyses, Economic Geology, 97(1), 73–91, doi:10.2113/gsecongeo.97.1.73, 2002.

Boiron, M. C., Cathelineau, M., Banks, D. A., Buschaert, S., Fourcade, S., Coulibaly, Y., Michelot, J. L. and Boyce, A.: Fluid transfers at a basement/cover interface Part II. Large-scale introduction of chlorine into the basement by Mesozoic basinal brines, Chemical Geology, 192, 121–140, 2002.

Bonnetti, C., Cuney, M., Michels, R., Truche, L., Malartre, F., Liu, X. and Yang, J.: The Multiple Roles of Sulfate-Reducing Bacteria and Fe-Ti Oxides in the Genesis of the Bayinwula Roll Front-Type Uranium Deposit, Erlian Basin, NE China, Economic Geology, 110(4), 1059–1081, doi:10.2113/econgeo.110.4.1059, 2015.

Bonnetti, C., Liu, X., Zhaobin, Y., Cuney, M., Michels, R., Malartre, F., Mercadier, J. and Cai, J.: Coupled uranium mineralisation and bacterial sulphate reduction for the genesis of the Baxingtu sandstone-hosted U deposit, SW Songliao Basin, NE China, Ore Geology Reviews, 82, 108–129, doi:10.1016/j.oregeorev.2016.11.013, 2017.

Bonnetti, C., Zhou, L., Riegler, T., Brugger, J. and Fairclough, M.: Large S isotope and trace element fractionations in pyrite of uranium roll front systems result from internally-driven biogeochemical cycle, Geochimica et Cosmochimica Acta, S0016703720303240, doi:10.1016/j.gca.2020.05.019, 2020.

Bosze, S. and Rakovan, J.: Surface-structure-controlled sectoral zoning of the rare earth elements in fluorite from Long Lake, New York, and Bingham, New Mexico, USA, Geochimica et Cosmochimica Acta, 66(6), 997–1009, doi:10.1016/S0016-7037(01)00822-5, 2002.

Brigaud, B., Bonifacie, M., Pagel, M., Blaise, T., Calmels, D., Haurine, F. and Landrein, P.: Past hot fluid flows in limestones detected by Δ47–(U-Pb) and not recorded by other geothermometers, Geology, 48(9), 851–856, doi:10.1130/G47358.1, 2020.

Burisch, M., Walter, B. F. and Markl, G.: Silicification of Hydrothermal Gangue Minerals in Pb-Zn-Cu-Fluorite-Quartz-Baryte Veins, The Canadian Mineralogist, 55(3), 501–514, doi:10.3749/canmin.1700005, 2017.

Cai, C., Dong, H., Li, H., Xiao, X., Ou, G. and Zhang, C.: Mineralogical and geochemical evidence for coupled bacterial uranium mineralization and hydrocarbon oxidation in the Shashagetai deposit, NW China, Chemical Geology, 236(1–2), 167–179, doi:10.1016/j.chemgeo.2006.09.007, 2007.

Campbell, K. M., Kukkadapu, R. K., Qafoku, N. P., Peacock, A. D., Lesher, E., Williams, K. H., Bargar, J. R., Wilkins, M. J., Figueroa, L., Ranville, J., Davis, J. A. and Long, P. E.: Geochemical, mineralogical and microbiological characteristics of sediment from a naturally reduced zone in a uranium-contaminated aquifer, Applied Geochemistry, 27(8), 1499–1511, doi:10.1016/j.apgeochem.2012.04.013, 2012.

Cardon, O.: Datation Re-Os sur pyrite et traçage des sources des métaux dans des gisements de type porphyre et épithermal neutre: Exemple des gisements de Bolcana, Troita et Magura, Monts Apuseni, Roumanie, Thèse de doctorat, Université Henri Poincaré, Nancy I., 2007.

Cathelineau, M., Boiron, M.-C., Fourcade, S., Ruffet, G., Clauer, N., Belcourt, O., Coulibaly, Y., Banks, D. A. and Guillocheau, F.: A major Late Jurassic fluid event at the basin/basement unconformity in western France: 40Ar/39Ar and K–Ar dating, fluid chemistry, and related geodynamic context, Chemical Geology, 322–323, 99–120, doi:10.1016/j.chemgeo.2012.06.008, 2012.

Chatagnon, B., Galland, D., Gloux, P. and Méary, A.: L'lon Paramagnétique Tm2+ dans la Fluorite : Un Témoin de la Radioactivité dans le Gisement, Mineralium Deposita, 17(3), doi:10.1007/BF00204469, 1982.

Cherniak, D. J., Zhang, X. Y., Wayne, N. K. and Watson, E. B.: Sr, Y, and REE diffusion in fluorite, Chemical Geology, 181(1–4), 99–111, doi:10.1016/S0009-2541(01)00267-4, 2001.

Chi, G., Li, Z., Chu, H., Bethune, K. M., Quirt, D. H., Ledru, P., Normand, C., Card, C., Bosman, S., Davis, W. J. and Potter, E. G.: A shallow-burial mineralization model for the unconformity-related uranium deposits in the Athabasca basin, Economic Geology, 113(5), 1209–1217, doi:10.5382/econgeo.2018.4588, 2018.

De Bonis, A., Santagata, A., Galasso, A., Sansone, M. and Teghil, R.: Femtosecond laser ablation of CaF2: Plasma characterization and thin films deposition, Applied Surface Science, 302, 145–148, doi:10.1016/j.apsusc.2013.09.089, 2014.

Deng, X.-D. and Li, J.-W.: Mineralogy and 40Ar/39Ar geochronology of supergene Mn-oxides in the Dongxiangqiao deposit, Hunan Province, South China, Mineralogy and Petrology, 111(2), 253–265, doi:10.1007/s00710-016-0466-y, 2017.

Dill, H. G. and Weber, B.: Accessory minerals of fluorite and their implication regarding the environment of formation (Nabburg–Wölsendorf fluorite district, SE Germany), with special reference to fetid fluorite (“Stinkspat”), Ore Geology Reviews, 37(2), 65–86, doi:10.1016/j.oregeorev.2010.01.004, 2010.

Dill, H. G., Hansen, B. T. and Weber, B.: REE contents, REE minerals and Sm/Nd isotopes of granite- and unconformity-related fluorite mineralization at the western edge of the Bohemian Massif: With special reference to the Nabburg-Wölsendorf District, SE Germany, Ore Geology Reviews, 40(1), 132–148, doi:10.1016/j.oregeorev.2011.06.003, 2011.

Ding, T., Valkiers, S., Kipphardt, H., De Bièvre, P., Taylor, P. D. P., Gonfiantini, R. and Krouse, R.: Calibrated sulfur isotope abundance ratios of three IAEA sulfur isotope reference materials and V-CDT with a reassessment of the atomic weight of sulfur, Geochimica et Cosmochimica Acta, 65(15), 2433–2437, doi:10.1016/S0016-7037(01)00611-1, 2001.

Elisha, B., Nuriel, P., Kylander-Clark, A. and Weinberger, R.: Towards in-situ U–Pb dating of dolomites, Geochronology Discussions, 1–17, doi:10.5194/gchron-2020-19, 2020.

European Commission. Study on the review of the list of critical raw materials. Final report. EU publications, Report, 92 pages, 2017.

Evans, N. J., Wilson, N. S. F., Cline, J. S., McInnes, B. I. A. and Byrne, J.: Fluorite (U–Th)/He thermochronology: Constraints on the low temperature history of Yucca Mountain, Nevada, Applied Geochemistry, 20(6), 1099–1105, doi:10.1016/j.apgeochem.2005.02.008, 2005.

Galindo, C., Tornos, F., Darbyshire, D. P. F. and Casquet, C.: The age and origin of the barite-fluorite (Pb-Zn) veins of the Sierra del Guadarrama (Spanish Central System, Spain): a radiogenic (Nd, Sr) and stable isotope study, Chemical Geology, 112(3–4), 351–364, doi:10.1016/0009-2541(94)90034-5, 1994.

Gigon, J., Deloule, E., Mercadier, J., Huston, D. L., Richard, A., Annesley, I. R., Wygralak, A. S., Skirrow, R. G., Mernagh, T. P. and Masterman, K.: Tracing metal sources for the giant McArthur River Zn-Pb deposit (Australia) using lead isotopes, Geology, 48(5), 478–482, doi:10.1130/G47001.1, 2020.

Gigoux, M., Delpech, G., Guerrot, C., Pagel, M., Augé, T., Négrel, P. and Brigaud, B.: Evidence for an Early Cretaceous mineralizing event above the basement/sediment unconformity in the intracratonic Paris Basin: paragenetic sequence and Sm-Nd dating of the world-class Pierre-Perthuis stratabound fluorite deposit, Mineralium Deposita, 50(4), 455–463, doi:10.1007/s00126-015-0592-1, 2015.

Gigoux, M., Brigaud, B., Pagel, M., Delpech, G., Guerrot, C., Augé, T. and Négrel, P.: Genetic constraints on world-class carbonate- and siliciclastic-hosted stratabound fluorite deposits in Burgundy (France) inferred from mineral paragenetic sequence and fluid inclusion studies, Ore Geology Reviews, 72, 940–962, doi:10.1016/j.oregeorev.2015.09.013, 2016.

Gleadow, A. J. W.: Fission-track dating methods: What are the real alternatives?, Nuclear Tracks, 5(1–2), 3–14, doi:10.1016/0191-278X(81)90021-4, 1981.

Gogoll, S., Stenzel, E., Johansen, H., Reichling, M. and Matthias, E.: Laser-damage of cleaved and polished CaF2 at 248 nm, Nuclear Instruments and Methods in Physics Research Section B: Beam Interactions with Materials and Atoms, 116(1–4), 279–283, doi:10.1016/0168-583X(96)00061-4, 1996.

Grønlie, A., Harder, V. and Roberts, D.: Preliminary fission-track ages of fluorite mineralisation along fracture zones, inner Trondheimsfjord, Central Norway, Norsk geologisk tidsskrift, 6, 1990.

Guillocheau, F.: Evolution tectonique méso-cénozoïque du bassin de Paris: contraintes stratigraphiques 3D, Geodinamica Acta, 13(4), 189–245, doi:10.1016/S0985-3111(00)00118-2, 2000.

Guillong, M., Wotzlaw, J.-F., Looser, N. and Laurent, O.: Evaluating the reliability of U–Pb laser ablation inductively coupled plasma mass spectrometry (LA-ICP-MS) carbonate geochronology: matrix issues and a potential calcite validation reference material, Geochronology, 2(1), 155–167, doi:10.5194/gchron-2-155-2020, 2020.

Heim, C., Lausmaa, J., Sjövall, P., Toporski, J., Dieing, T., Simon, K., Hansen, B. T., Kronz, A., Arp, G., Reitner, J. and Thiel, V.: Ancient microbial activity recorded in fracture fillings from granitic rocks (Äspö Hard Rock Laboratory, Sweden): Ancient microbial activity recorded in fracture fillings, Geobiology, 10(4), 280–297, doi:10.1111/j.1472-4669.2012.00328.x, 2012.

Hill, C. A., Polyak, V. J., Asmerom, Y. and Provencio, P. P.: Constraints on a Late Cretaceous uplift, denudation, and incision of the Grand Canyon region, southwestern Colorado Plateau, USA, from U-Pb dating of lacustrine limestone, Tectonics, 35(4), 896–906, doi:10.1002/2016TC004166, 2016.

Hough, G., Swapp, S., Frost, C. and Fayek, M.: Sulfur Isotopes in Biogenically and Abiogenically Derived Uranium Roll-Front Deposits, Economic Geology, 114(2), 353–373, doi:10.5382/econgeo.2019.4634, 2019.

Ingham, E. S., Cook, N. J., Cliff, J., Ciobanu, C. L. and Huddleston, A.: A combined chemical, isotopic and microstructural study of pyrite from roll-front uranium deposits, Lake Eyre Basin, South Australia, Geochimica et Cosmochimica Acta, 125, 440–465, doi:10.1016/j.gca.2013.10.017, 2014.

Jia, T. Q., Li, X. X., Feng, D. H., Cheng, C. F., Li, R. X., Chen, H. and Xu, Z. Z.: Theoretical and experimental study on femtosecond laser induced damage in CaF2 crystals, Applied Physics A, 81(3), 645–649, doi:10.1007/s00339-004-2685-z, 2005.

Jochum, K. P., Weis, U., Stoll, B., Kuzmin, D., Yang, Q., Raczek, I., Jacob, D. E., Stracke, A., Birbaum, K., Frick, D. A., Günther, D. and Enzweiler, J.: Determination of Reference Values for NIST SRM 610-617 Glasses Following ISO Guidelines, Geostandards and Geoanalytical Research, 35(4), 397–429, doi:10.1111/j.1751-908X.2011.00120.x, 2011.

Johansen, H., Gogoll, S., Stenzel, E. and Reichling, M.: Scanning electron microscopical inspection of uncoated CaF2 single crystals, Physica Status Solidi (a), 150(2), 613–624, doi:10.1002/pssa.2211500205, 1995.

Kahou, Z. S., Brichau, S., Poujol, M., Duchêne, S., Campos, E., Leisen, M., d'Abzac, F.-X., Riquelme, R. and Carretier, S.: First U-Pb LA-ICP-MS in situ dating of supergene copper mineralization: case study in the Chuquicamata mining district, Atacama Desert, Chile, Mineralium Deposita, 1–14, doi:10.1007/s00126-020-00960-2, 2020.

Kawasaki, K. and Symons, D. T. A.: Paleomagnetism of fluorite veins in the Devonian St. Lawrence granite, Newfoundland, Canada, edited by F. Cook, Canadian Journal of Earth Sciences, 45(9), 969–980, doi:10.1139/E08-045, 2008.

Kempe, U., Plötze, M., Brachmann, A. and Böttcher, R.: Stabilisation of divalent rare earth elements in natural fluorite, Mineralogy and Petrology, 76, 213–234, 2002.

Kröger, F. A.: The incorporation of uranium in calcium fluoride, Physica, 14(7), 488, doi:10.1016/0031-8914(48)90019-6, 1948.

LaFlamme, C., Martin, L., Jeon, H., Reddy, S. M., Selvaraja, V., Caruso, S., Bui, T. H., Roberts, M. P., Voute, F., Hagemann, S., Wacey, D., Littman, S., Wing, B., Fiorentini, M. and Kilburn, M. R.: In situ multiple sulfur isotope analysis by SIMS of pyrite, chalcopyrite, pyrrhotite, and pentlandite to refine magmatic ore genetic models, Chemical Geology, 444, 1–15, doi:10.1016/j.chemgeo.2016.09.032, 2016.

Lanzirotti, A., Tappero, R. and Schulze, D. G.: Practical Application of Synchrotron-Based Hard X-Ray Microprobes in Soil Sciences, in Developments in Soil Science, vol. 34, pp. 27–72, Elsevier., 2010.

Lardeaux, J. M., Schulmann, K., Faure, M., Janoušek, V., Lexa, O., Skrzypek, E., Edel, J. B. and Štípská, P.: The Moldanubian Zone in the French Massif Central, Vosges/Schwarzwald and Bohemian Massif revisited: differences and similarities, Geological Society, London, Special Publications, 405(1), 7–44, doi:10.1144/SP405.14, 2014.

Lawson, M., Shenton, B. J., Stolper, D. A., Eiler, J. M., Rasbury, E. T., Becker, T. P., Phillips-Lander, C. M., Buono, A. S., Becker, S. P., Pottorf, R., Gray, G. G., Yurewicz, D. and Gournay, J.: Deciphering the diagenetic history of the El Abra Formation of eastern Mexico using reordered clumped isotope temperatures and U-Pb dating, GSA Bulletin, 130(3–4), 617–629, doi:10.1130/B31656.1, 2018.

Leach, D. L., Sangster, D. F., Kelley, K. D., Large, R. R., Garven, G., Allen, C. R., Gutzmer, J. and Walters, S.: Sediment-hosted lead-zinc deposits: A global perspective, Economic Geology, One Hundredth Anniversary Volume(3), 561–607, doi:10.5382/AV100.18, 2005.

Lefort, J. P. and Agarwal, B. N. P.: Topography of the Moho undulations in France from gravity data: their age and origin, Tectonophysics, 350(3), 193–213, doi:10.1016/S0040-1951(02)00114-2, 2002.

Lovley, D. R., Phillips, E. J. P., Gorby, Y. A. and Landa, E. R.: Microbial reduction of uranium, Nature, 350(6317), 413–416, doi:10.1038/350413a0, 1991.

Machel, H. G.: Bacterial and thermochemical sulfate reduction in diagenetic settings - old and new insights, Sedimentary Geology, 140(1–2), 143–175, doi:10.1016/S0037-0738(00)00176-7, 2001.

Magnall, J. M., Gleeson, S. A., Stern, R. A., Newton, R. J., Poulton, S. W. and Paradis, S.: Open system sulphate reduction in a diagenetic environment – Isotopic analysis of barite (δ34S and δ18O) and pyrite (δ34S) from the Tom and Jason Late

Devonian Zn–Pb–Ba deposits, Selwyn Basin, Canada, Geochimica et Cosmochimica Acta, 180, 146–163, doi:10.1016/j.gca.2016.02.015, 2016.

Mangenot, X., Gasparrini, M., Rouchon, V. and Bonifacie, M.: Basin-scale thermal and fluid flow histories revealed by carbonate clumped isotopes (Δ47) - Middle Jurassic carbonates of the Paris Basin depocentre, Sedimentology, 65(1), 123–150, doi:10.1111/sed.12427, 2018.

Mark, D. F., Parnell, J., Kelley, S. P., Lee, M., Sherlock, S. C. and Carr, A.: Dating of Multistage Fluid Flow in Sandstones, Science, 309(5743), 2048–2051, doi:10.1126/science.1116034, 2005.

Markey, R., Stein, H. J. and Morgan, J. W.: Highly precise Re–Os dating for molybdenite using alkaline fusion and NTIMS, Talanta, 45(5), 935–946, doi:10.1016/S0039-9140(97)00198-7, 1998.

Martz, P., Mercadier, J., Perret, J., Villeneuve, J., Deloule, E., Cathelineau, M., Quirt, D., Doney, A. and Ledru, P.: Post-crystallization alteration of natural uraninites: Implications for dating, tracing, and nuclear forensics, Geochimica et Cosmochimica Acta, 249, 138–159, doi:10.1016/j.gca.2019.01.025, 2019.

Mathur, R., Ruiz, J., Titley, S., Gibbins, S. and Margotomo, W.: Different crustal sources for Au-rich and Au-poor ores of the Grasberg Cu–Au porphyry deposit, Earth and Planetary Science Letters, 183(1–2), 7–14, doi:10.1016/S0012-821X(00)00256-9, 2000.

Medjoubi, K., Leclercq, N., Langlois, F., Buteau, A., Lé, S., Poirier, S., Mercère, P., Sforna, M. C., Kewish, C. M. and Somogyi, A.: Development of fast, simultaneous and multi-technique scanning hard X-ray microscopy at Synchrotron Soleil, Journal of Synchrotron Radiation, 20(2), 293–299, doi:10.1107/S0909049512052119, 2013.

Moscati, R. J. and Neymark, L. A.: U–Pb geochronology of tin deposits associated with the Cornubian Batholith of southwest England: Direct dating of cassiterite by in situ LA-ICPMS, Mineralium Deposita, 55(1), 1–20, doi:10.1007/s00126-019-00870-y, 2020.

Nakai, S., Halliday, A. N., Kesler, S. E., Jones, H. D., Kyle, J. R. and Lane, T. E.: Rb-Sr dating of sphalerites from Mississippi Valley-type (MVT) ore deposits, Geochimica et Cosmochimica Acta, 57(2), 417–427, doi:10.1016/0016-7037(93)90440-8, 1993.

Nuriel, P., Rosenbaum, G., Uysal, T. I., Zhao, J., Golding, S. D., Weinberger, R., Karabacak, V. and Avni, Y.: Formation of fault-related calcite precipitates and their implications for dating fault activity in the East Anatolian and Dead Sea fault zones, Geological Society, London, Special Publications, 359(1), 229–248, doi:10.1144/SP359.13, 2011.

Nuriel, P., Weinberger, R., Kylander-Clark, A. R. C., Hacker, B. R. and Craddock, J. P.: The onset of the Dead Sea transform based on calcite age-strain analyses, Geology, 45(7), 587–590, doi:10.1130/G38903.1, 2017.

Nuriel, P., Miller, D. M., Schmidt, K. M., Coble, M. A. and Maher, K.: Ten-million years of activity within the Eastern California Shear Zone from U–Pb dating of fault-zone opal, Earth and Planetary Science Letters, 521, 37–45, doi:10.1016/j.epsl.2019.05.047, 2019.

O. Horon, M.-M., Megnien, C. and Lefavrais-Raymond, A.: Carte géologique de la France, feuille 466 : Avallon, 1966.

Pagel, M., Bonifacie, M., Schneider, D. A., Gautheron, C., Brigaud, B., Calmels, D., Cros, A., Saint-Bezar, B., Landrein, P., Sutcliffe, C., Davis, D. and Chaduteau, C.: Improving paleohydrological and diagenetic reconstructions in calcite veins and breccia of a sedimentary basin by combining Δ47 temperature, δ18Owater and U-Pb age, Chemical Geology, 481, 1–17, doi:10.1016/j.chemgeo.2017.12.026, 2018.

Paton, C., Hellstrom, J., Paul, B., Woodhead, J. and Hergt, J.: Iolite: Freeware for the visualisation and processing of mass spectrometric data, Journal of Analytical Atomic Spectrometry, 26(12), 2508, doi:10.1039/c1ja10172b, 2011.

Peverelli, V., Ewing, T., Rubatto, D., Wille, M., Berger, A., Villa, I. M., Lanari, P., Pettke, T. and Herwegh, M.: U–Pb geochronology of epidote by LA–ICP–MS as a tool for dating hydrothermal-vein formation, preprint, SIMS, LA-ICP-MS., 2020.

Pi, T., Solé, J., Golzarri, J., Rickards, J. and Espinosa, G.: Autoradiography of geological fluorite samples for determination of uranium and thorium distribution using nuclear track methodology, Revista mexicana de física, 53, 57–60, 2007.

Piccione, G., Rasbury, E. T., Elliott, B. A., Kyle, J. R., Jaret, S. J., Acerbo, A. S., Lanzirotti, A., Northrup, P., Wooton, K. and Parrish, R. R.: Vein fluorite U-Pb dating demonstrates post–6.2 Ma rare-earth element mobilization associated with Rio Grande rifting, Geosphere, 15(6), 1958–1972, doi:10.1130/GES02139.1, 2019.

Rackley, R. I.: Environment of Wyoming Tertiary uranium deposits, AAPG Bulletin, 56(4), 755–774, 1972.

Rafique, M. S., Bashir, S., Husinsky, W., Hobro, A. and Lendl, B.: Surface analysis correlated with the Raman measurements of a femtosecond laser irradiated CaF2, Applied Surface Science, 258(7), 3178–3183, doi:10.1016/j.apsusc.2011.11.059, 2012.

Rasbury, E. T. and Cole, J. M.: Directly dating geologic events: U-Pb dating of carbonates, Reviews of Geophysics, 47(3), 1–27, doi:10.1029/2007RG000246, 2009.

Recker, K.: Über den Einbau von Uran in CaF2, Deutsche Mineralogische Gesellschaft 5. bis 12 September 1960 in Bonn, Angewandte Chemie, 73(1), 39–41, doi:10.1002/ange.19610730118, 1961.

Reichling, M., Johansen, H., Gogoll, S., Stenzel, E. and Matthias, E.: Laser-stimulated desorption and damage at polished CaF2 surfaces irradiated with 532 nm laser light, Nuclear Instruments and methods in physics research, 628–633, 1994.

Roberts, N. M. W., Rasbury, E. T., Parrish, R. R., Smith, C. J., Horstwood, M. S. A. and Condon, D. J.: A calcite reference material for LA-ICP-MS U-Pb geochronology, Geochemistry, Geophysics, Geosystems, 18(7), 2807–2814, doi:10.1002/2016GC006784, 2017.

Roberts, N. M. W., Drost, K., Horstwood, M. S. A., Condon, D. J., Chew, D., Drake, H., Milodowski, A. E., McLean, N. M., Smye, A. J., Walker, R. J., Haslam, R., Hodson, K., Imber, J., Beaudoin, N. and Lee, J. K.: Laser ablation inductively coupled plasma mass spectrometry (LA-ICP-MS) U-Pb carbonate geochronology: strategies, progress, and limitations, Geochronology, 2(1), 33–61, doi:10.5194/gchron-2-33-2020, 2020.

Schneider, C. A., Rasband, W. S. and Eliceiri, K. W.: NIH Image to ImageJ: 25 years of image analysis, Nat Methods, 9(7), 671–675, doi:10.1038/nmeth.2089, 2012.

Sizaret, S.: Genèse du Système Hydrothermal à Fluorine-Barytine-Fer de Chaillac, (Indre, France), Thèse de doctorat, Université d'Orléans., 2006.

Solé, V. A., Papillon, E., Cotte, M., Walter, Ph. and Susini, J.: A multiplatform code for the analysis of energy-dispersive X-ray fluorescence spectra, Spectrochimica Acta Part B: Atomic Spectroscopy, 62(1), 63–68, doi:10.1016/j.sab.2006.12.002, 2007.

Somogyi, A., Medjoubi, K., Baranton, G., Le Roux, V., Ribbens, M., Polack, F., Philippot, P. and Samama, J.-P.: Optical design and multi-length-scale scanning spectro-microscopy possibilities at the Nanoscopium beamline of Synchrotron Soleil, Journal of Synchrotron Radiation, 22(4), 1118–1129, doi:10.1107/S1600577515009364, 2015.

Soulé de Lafont, D. and Lhégu, J.: Les gisements stratiformes du Morvan (sud-est du bassin de Paris, France), 26 CGI, Paris7-BRGM fascicule sur les gisements Français E2, 40 p, 1980.

Stacey, J. S. and Kramers, J. D.: Approximation of terrestrial lead isotope evolution by a two-stage model, Earth and Planetary Science Letters, 26, 207–221, 1975.

Stein, H. J., Markey, R. J., Morgan, J. W., Hannah, J. L. and Schersten, A.: The remarkable Re-Os chronometer in molybdenite: how and why it works, Terra Nova, 13(6), 479–486, doi:10.1046/j.1365-3121.2001.00395.x, 2001.

Symons, D. T. A.: Paleomagnetism and the Late Jurassic genesis of the Illinois-Kentucky fluorspar deposits, Economic Geology, 89(3), 438–449, doi:10.2113/gsecongeo.89.3.438, 1994.

Symons, D. T. A., Kawasaki, K., Tornos, F., Velasco, F. and Rosales, I.: Temporal constraints on genesis of the Caravia-Berbes fluorite deposits of Asturias, Spain, from paleomagnetism, Ore Geology Reviews, 80, 754–766, doi:10.1016/j.oregeorev.2016.08.020, 2017.

Vermeesch, P.: IsoplotR: A free and open toolbox for geochronology, Geoscience Frontiers, 9(5), 1479–1493, doi:10.1016/j.gsf.2018.04.001, 2018.

Vialette, Y.: Age des granites du Massif Central, Bulletin de la Société Géologique de France, S7-XV(3–4), 260–270, doi:10.2113/gssgfbull.S7-XV.3-4.260, 1973.

Vochten, R., Esmans, E. and Vermeirsch, W.: Study of the solid and gaseous inclusions in the fluorites from Wölsendorf (Bavaria, F.R. of Germany) and Margnac (Haute Vienne, France) by microprobe and mass spectrometry, Chemical Geology, 20, 253–263, 1977.

Walter, B. F., Gerdes, A., Kleinhanns, I. C., Dunkl, I., von Eynatten, H., Kreissl, S. and Markl, G.: The connection between hydrothermal fluids, mineralization, tectonics and magmatism in a continental rift setting: Fluorite Sm-Nd and hematite and carbonates U-Pb geochronology from the Rhinegraben in SW Germany, Geochimica et Cosmochimica Acta, 240, 11–42, doi:10.1016/j.gca.2018.08.012, 2018.

Wolff, R., Dunkl, I., Kempe, U. and von Eynatten, H.: The Age of the Latest Thermal Overprint of Tin and Polymetallic Deposits in the Erzgebirge, Germany: Constraints from Fluorite (U-Th-Sm)/He Thermochronology, Economic Geology, 110(8), 2025–2040, doi:10.2113/econgeo.110.8.2025, 2015.

Wolff, R., Dunkl, I., Kempe, U., Stockli, D., Wiedenbeck, M. and von Eynatten, H.: Variable helium diffusion characteristics in fluorite, Geochimica et Cosmochimica Acta, 188, 21–34, doi:10.1016/j.gca.2016.05.029, 2016.

Wu, Y.-F., Fougerouse, D., Evans, K., Reddy, S. M., Saxey, D. W., Guagliardo, P. and Li, J.-W.: Gold, arsenic, and copper zoning in pyrite: A record of fluid chemistry and growth kinetics, Geology, 47(7), 641–644, doi:10.1130/G46114.1, 2019.

Xing, Y., Etschmann, B., Liu, W., Mei, Y., Shvarov, Y., Testemale, D., Tomkins, A. and Brugger, J.: The role of fluorine in hydrothermal mobilization and transportation of Fe, U and REE and the formation of IOCG deposits, Chemical Geology, 504, 158–176, doi:10.1016/j.chemgeo.2018.11.008, 2019.

Yi, Z.-J., Tan, K.-X., Tan, A.-L., Yu, Z.-X. and Wang, S.-Q.: Influence of environmental factors on reductive bioprecipitation of uranium by sulfate reducing bacteria, International Biodeterioration & Biodegradation, 60(4), 258–266, doi:10.1016/j.ibiod.2007.04.001, 2007.